

# Self-gravity effects of ultralight boson clouds formed by black hole superradiance

Taillte May,<sup>1,2,\*</sup> William E. East,<sup>1,†</sup> and Nils Siemonsen<sup>3,4,‡</sup>

<sup>1</sup>*Perimeter Institute for Theoretical Physics, Waterloo, Ontario N2L 2Y5, Canada*

<sup>2</sup>*Department of Physics & Astronomy, University of Waterloo, Waterloo, Ontario N2L 3G1 Canada*

<sup>3</sup>*Princeton Gravity Initiative, Princeton University, Princeton New Jersey 08544, USA*

<sup>4</sup>*Department of Physics, Princeton University, Princeton, New Jersey 08544, USA*

(Dated: Wednesday 30<sup>th</sup> October, 2024)

Oscillating clouds of ultralight bosons can grow around spinning black holes through superradiance, extracting energy and angular momentum, and eventually dissipating through gravitational radiation. Gravitational wave detectors like LIGO, Virgo, KAGRA, and LISA can thus probe the existence of ultralight bosons. In this study, we use fully general-relativistic solutions of the black hole-boson cloud systems to study the self-gravity effects of scalar and vector boson clouds, making only the simplifying assumption that the spacetime is axisymmetric (essentially corresponding to taking an oscillation average). We calculate the self-gravity shift in the cloud oscillation frequency, which determines the frequency evolution of the gravitational wave signal, finding that this effect can be up to twice as large in the relativistic regime compared to non-relativistic estimates. We use this to improve the **superrad** waveform model, and estimate that this reduces the theoretical phase error to a few cycles over the characteristic timescale of the gravitational wave emission timescale for the louder vector boson signals. We also perform an analysis of the spacetime geometry of these systems, calculating how the cloud changes the innermost stable circular orbit and light-ring around the black hole.

## I. INTRODUCTION

An intriguing possibility of recent focus is the prospect of using observations of black holes and gravitational waves to probe the existence of ultralight bosons. There are several theoretical motivations for considering scalar and vector particles that are weakly coupled to the Standard Model. The QCD axion is a (pseudo) scalar example [1, 2], whose mass is observationally constrained to  $m_b \leq 10^{-3}$  eV [3], and for some models is theoretically expected to be  $m_b \sim 10^{-10}$  eV [4–6]. Axions, along with dark photons [7–10], have been considered as potential dark matter candidates; string theory also features ultralight axion-like particles [11], as well as vector bosons [12] in the mass range  $10^{-33}$  to  $10^{-10}$  eV.

Black holes can produce ultralight bosons through the superradiant mechanism. A scattering field can extract rotational energy from a black hole if it satisfies the superradiance condition,  $\omega < m\Omega_H$ , where  $\omega$  is the angular frequency of the field,  $m$  is its azimuthal mode number, and  $\Omega_H$  is frequency of the black hole horizon [13–15]. A field in a bound state that satisfies the superradiance condition will be continuously amplified through this process, and grows exponentially with time. In the absence of other couplings, the resulting boson cloud eventually spins down the black hole sufficiently to saturate the superradiance condition; after this, there is minimal flux through the black hole horizon and the cloud will dissipate through gravitational radiation. This process is possible in principle for a bosonic field with any mass,

though the instability rate is only astrophysically relevant if the Compton wavelength of the field is roughly comparable to the black hole’s radius. This is equivalent to  $\alpha \equiv Gm_b M_{\text{BH}}/(c^3 \hbar) \sim 1$ , where  $m_b$  is the boson’s mass and  $M_{\text{BH}}$  the black hole’s mass.

The black hole superradiant instability occurs for minimally coupled ultralight scalar and vector bosons<sup>1</sup>, therefore, it can probe particles with arbitrarily weak couplings to Standard Model particles, complementing terrestrial experiments. Black hole spin measurements and gravitational waves from binary black hole mergers can be used to place constraints on the existence of ultralight bosons [20–25]. The gravitational waves emitted by a dissipating boson cloud fall in the LIGO-Virgo-KAGRA sensitivity band [26–29] for boson masses in the range from  $10^{-13}$  to  $10^{-11}$  eV, while boson masses in between  $10^{-18}$  and  $10^{-15}$  eV correspond to LISA’s future sensitivity range [30]. Stochastic background searches and blind continuous wave searches can be used to look for signals for some unknown population of black holes that has undergone the superradiant instability [5, 20–22, 31–39], though placing constraints in the absence of a detection requires one to make assumptions about the (largely unknown) black hole population. Alternatively, one can consider targeting specific known black holes [40]. In particular, performing follow-up searches of the merger remnants of observed binary black hole mergers has the

<sup>1</sup> The superradiant instability can also occur for massive spin-2 fields [16, 17], though the observational implications are complicated by the fact that in this case there is another instability that occurs even for non-spinning black holes [18]. This instability is even faster in much of the parameter space and the (potentially model-dependent) nonlinear evolution has only begun to be explored [19].

\* [tmay@perimeterinstitute.ca](mailto:tmay@perimeterinstitute.ca)

† [weast@perimeterinstitute.ca](mailto:weast@perimeterinstitute.ca)

‡ [nils.siemonsen@princeton.edu](mailto:nils.siemonsen@princeton.edu)

advantage that the properties of a merger remnant can be estimated from the merger signal, and so specific boson masses can be constrained with minimal assumptions [41–43]. However, this is feasible only for the fastest evolving boson clouds and loudest gravitational wave signals. For these, it is important to have a relativistically accurate gravitational waveform model, a crucial aspect of which we develop in this work.

The gravitational wave signal from a superradiant cloud is mostly monochromatic, but with a small upward drift in the frequency due to the changing mass of the boson cloud. Not accounting for this limits the timescales over which the signal can be coherently tracked by gravitational wave search methods. The frequency shift due to the self-gravity of the cloud was first calculated in Refs. [24] and [41, 44], in the Newtonian limit of the fastest growing vector and scalar modes, respectively. In Ref. [45], this was extended to higher azimuthal modes and compared to a quasi-relativistic calculation introduced in Ref. [46]. The latter is still based on evaluating the Newtonian expressions for the frequency shift, but employs relativistic test-field solutions to calculate the energy density. More recently, Ref. [47] used relativistic perturbation theory to estimate this effect, but still treating the perturbation from the cloud’s self-gravity in terms of a Newtonian potential, and found an improvement from the non-relativistic limit.

As we show below, these previous non-relativistic estimates for the frequency shift can be off by an order-one factor in the relativistic regime. In this work, we account for the self-gravity effects of the boson cloud around a black hole in a fully relativistic way by leveraging stationary spacetime solutions describing black holes with synchronized complex scalar or vector clouds, first constructed in Refs. [48–51]. We utilize these to determine the cloud mass dependence of the cloud frequency, and hence, the frequency of the gravitational wave signal in an oscillation-average approximation for  $m = 1$  scalar and vector boson clouds. Using this, we update the waveform model `SuperRad`<sup>2</sup>, introduced in Ref. [45]. With these results, the accumulated phase error is reduced by several orders of magnitude, and for vector bosons is on the order of one radian or smaller over the characteristic timescale of the gravitational wave signal in much of the parameter space.

The black hole-boson cloud solutions can also be used to determine how the cloud changes the black hole’s spacetime, and hence, how it affects the redshift, lensing, shadows, etc. associated with the system, as studied in Refs. [49, 52, 53]. Here, we compare the geometry of the scalar cloud case to the vector case in terms of the effect on quantities like the innermost stable circular orbit (ISCO) radius and light ring, and comment on how this may affect measurements of black hole spin.

The layout of this paper is as follows. In Sec. II, we provide some background on the non-relativistic treatment of this problem, and some details on the oscillation-averaged approximation considered here. We describe how we numerically construct solutions in Sec. III, with more details included in the Appendices. We present our main results in Sec. IV, showing the relativistic correction to the frequency in Sec. IV A, with an updated estimate of the phase error in the superradiance waveform in Sec. IV B, as well as the effect of the presence of a boson cloud on the geometry in Sec. IV C. Finally, we conclude with a discussion of the implications of these results in Sec. V. In the following, we use geometrized units ( $G = c = 1$ ) and the unit-adjusted boson mass  $\mu \equiv m_b/\hbar$ .

## II. PRELIMINARIES

### A. Non-relativistic superradiance

In this section, we review the solutions describing boson clouds arising from superradiance in the non-relativistic limit and their associated timescales. This is to provide context for the results of this study, as well as to introduce some useful definitions.

First, we note that the non-relativistic limit for black hole superradiance corresponds to the regime  $\alpha \equiv M_{\text{BH}}\mu \ll 1$ , where the characteristic length scale of the black hole is much smaller than that of the cloud [the former being given by  $\sim \alpha/\mu$  and the latter by  $\sim 1/(\alpha\mu)$ ]. In the non-relativistic limit, the governing test-field equations can be solved analytically [24, 54–56] to obtain a spectrum of superradiantly unstable modes. These modes are analogous to the energy states in the hydrogen atom, and therefore, are also labelled by the numbers  $\ell$ ,  $m$ , and  $n$ , corresponding to the orbital angular number, azimuthal number, and number of radial nodes. The frequencies of the bound states for a boson field around a black hole are given by

$$\omega \approx \mu \left( 1 - \frac{\alpha^2}{2(n + \ell + 1)^2} + \mathcal{O}(\alpha^3) \right). \quad (1)$$

In this study, we will focus on the  $(\ell, m, n) = (1, 1, 0)$  mode for the scalar case and the  $(\ell, m, n) = (0, 1, 0)$  for the vector case, which correspond to the fastest growing modes at the respective spins. The cloud growth timescale for the fastest growing mode, to leading order in  $\alpha$ , scales as [54]

$$\tau_{\text{inst.}}^{\text{sca}} \sim \frac{1}{\alpha^9(m\Omega_H - \omega)}, \quad (2)$$

in the scalar case. In the vector case the fastest growing mode has a growth timescale that scales as [24]

$$\tau_{\text{inst.}}^{\text{vec}} \sim \frac{1}{\alpha^7(m\Omega_H - \omega)}, \quad (3)$$

<sup>2</sup> Available at <https://www.bitbucket.org/weast/superrad>.

where in this limit  $\omega \approx \mu \ll m\Omega_H$ . Once the cloud extracts a sufficient amount of angular momentum from the black hole, the superradiance condition is nearly saturated  $\Omega_H \approx \omega/m$ , and the cloud dissipates through gravitational radiation. The emission timescale  $\tau_{\text{GW}}$  is the time for the cloud to decrease to half its original mass through gravitational dissipation after saturation. This emission timescale for the fastest growing (and dissipating) modes scale with  $\alpha$  to leading order as follows [24, 56]:

$$\begin{aligned}\tau_{\text{GW}}^{\text{sca}} &\sim \alpha^{-14} \left( \frac{M_{\text{BH}}^2}{M_{\text{cloud}}} \right)_{t=t_{\text{sat}}}, \\ \tau_{\text{GW}}^{\text{vec}} &\sim \alpha^{-10} \left( \frac{M_{\text{BH}}^2}{M_{\text{cloud}}} \right)_{t=t_{\text{sat}}},\end{aligned}\quad (4)$$

where the mass of the cloud  $M_{\text{cloud}}$  is evaluated at the time it reaches its maximum. Note that  $\tau_{\text{inst}} \ll \tau_{\text{GW}}$ . As indicated by the above scalings, vector boson clouds can grow and dissipate on much shorter timescales than scalar clouds.

### B. Non-relativistic frequency shift

Generally, there will be a contribution to the gravitational binding energy due to the boson cloud's self-gravity, which was neglected in the above expressions. Most notably, the cloud's frequency  $\omega$  (and hence, also the gravitational wave frequency) is shifted by an amount dependent on the cloud's mass  $M_{\text{cloud}}$ . We define  $\Delta\omega = \omega(M_{\text{cloud}}) - \omega(M_{\text{cloud}} = 0)$  to be this cloud mass dependent frequency shift. As the cloud dissipates through gravitational wave emission and  $M_{\text{cloud}}$  decreases, this leads to a gradual increase of the gravitational wave frequency over time. Following Refs. [24, 41, 44, 45], this frequency shift was determined in the non-relativistic regime. There, cloud's energy density  $\rho(\mathbf{r})$  sources the Newtonian potential

$$U(\mathbf{r}) = - \int d^3\mathbf{r}' \frac{\rho(\mathbf{r}')}{|\mathbf{r} - \mathbf{r}'|}. \quad (5)$$

The leading order in  $\alpha$  expression for the energy density of the cloud  $\rho(\mathbf{r})$  [where, in this limit, the cloud mass is  $M_{\text{cloud}} = \int d^3\mathbf{r} \rho(\mathbf{r})$ ] is given by  $\rho(\mathbf{r}) = \mu^2 \psi(\mathbf{r})^2$  and  $\rho(\mathbf{r}) = \mu^2 \mathcal{A}_a(\mathbf{r}) \mathcal{A}^a(\mathbf{r})$ , using the analytic non-relativistic solution of the cloud distributions  $\psi(\mathbf{r})$  and  $\mathcal{A}^a(\mathbf{r})$  from, e.g., Refs. [24, 56]. Here and in the following, we use  $\mu$  interchangeably for the scalar and vector masses (as done also for  $\omega$  and  $m$ ). Note also, we dropped the time-dependencies of  $\psi(\mathbf{r})$  and  $\mathcal{A}^a(\mathbf{r})$ , since these integrate away as discussed below. The frequency shift is then

$$\begin{aligned}\Delta\omega \frac{M_{\text{cloud}}}{\mu} &\approx \int d^3\mathbf{r} \rho(\mathbf{r}) U(\mathbf{r}) \\ &= -2 \int d^3\mathbf{r} \int_{|\mathbf{r}'| < |\mathbf{r}|} d^3\mathbf{r}' \frac{\rho(\mathbf{r}) \rho(\mathbf{r}')}{|\mathbf{r} - \mathbf{r}'|} = 2W,\end{aligned}\quad (6)$$

where  $W$  is the non-relativistic expression for the binding energy of the cloud<sup>3</sup>. We can then perform a multipole expansion for the denominator in Eq. (6). When  $|\mathbf{r}| \geq |\mathbf{r}'|$ , we have that

$$\frac{1}{|\mathbf{r} - \mathbf{r}'|} = \sum_{l=0}^{\infty} \sum_{m=-l}^l \left( \frac{|\mathbf{r}'|^l}{|\mathbf{r}|^{l+1}} \right) \frac{4\pi}{2l+1} Y_{lm}(\Omega) Y_{lm}^*(\Omega'), \quad (7)$$

where  $Y_{lm}(\Omega)$  are the spherical harmonics,  $\Omega$  denotes the two angles on the sphere, and \* indicates complex conjugation. In the monopole approximation, where only the first term ( $l = 0$ ) in this series is included, Eq. (6) gives

$$\Delta\omega \approx - \frac{2\mu}{M_{\text{cloud}}} \int d^3\mathbf{r} \int_{|\mathbf{r}'| < |\mathbf{r}|} d^3\mathbf{r}' \frac{\rho(\mathbf{r}) \rho(\mathbf{r}')}{|\mathbf{r}|}. \quad (8)$$

In Ref. [45], several higher multipoles were calculated and the error in the monopole approximation (when considered the leading order in  $\alpha$  term) is found to be at the percent level in the scalar case, and subleading in  $\alpha$  in the vector case. As noted above, after performing this integral, the time dependence of the potential drops out. The final result in the monopole and non-relativistic approximation is [45]

$$\Delta\omega_{\text{non-rel}}^{\text{sca}} \approx - \frac{93}{512} \frac{M_{\text{cloud}} \alpha^3}{M_{\text{BH}}^2}, \quad (9)$$

$$\Delta\omega_{\text{non-rel}}^{\text{vec}} \approx - \frac{5}{8} \frac{M_{\text{cloud}} \alpha^3}{M_{\text{BH}}^2}. \quad (10)$$

### C. Relativistic frequency shift

The aim of this work is to calculate the self-gravity effects of the cloud, including the frequency shift, in a relativistically accurate way. In principle, this could be calculated using black hole perturbation theory by solving for the metric perturbation due to the cloud, and then determining how this shifts the eigenfrequencies of the boson cloud solutions. However, given the intricacies of beyond-leading order black hole perturbation theory, here we opt instead to numerically solve the full governing Einstein equations. For a single (real) bosonic field, the presence of the cloud means that the spacetime is no longer exactly stationary or axisymmetric, so solving for the full, dynamical spacetimes while covering the parameter space (with the accuracy we require) would be infeasible without reducing the dimensionality of the problem. Instead, we calculate the self-gravity effects of the cloud in a related axisymmetric and stationary spacetime, where instead of considering a real scalar or

<sup>3</sup> N.B. the factor of two difference in Eq. (6) compared to some previous references, as discussed in Ref. [45].

vector field, we consider a complex field with a harmonic time and azimuthal dependence given by  $\sim e^{i(m\varphi - \omega t)}$ . This is equivalent to considering a superposition of two real bosonic fields (with identical masses) with a relative phase shift of  $\pi/2$ . In this sense, considering a stationary complex field instead of a real one is an oscillation-averaged approximation. When we further assume that the bosonic field saturates the black hole superradiance condition exactly ( $\omega = m\Omega_H$ ), and thus has no flux through the horizon, then one obtains the solutions found in Refs. [48–51].

Applying results from these stationary solutions to the gravitational wave-emitting cases is justified by the fact that the gravitational radiation timescale is always much longer than the oscillation period, and the energy density of the boson cloud solutions (in the Newtonian limit) is axisymmetric to a large degree. However, this does introduce a small theoretical error. We explicitly estimate this in Appendix C1a, and include this in our overall error estimates, as discussed below. We also compare the relativistic frequency calculation to the frequency obtained in a numerical relativity evolution without symmetry assumptions in Appendix C1b. We find the two are consistent, though the uncertainties in latter are significantly larger than the expected error in the former.

### III. METHODS

#### A. Construction of solutions

As in Refs. [48–51], we numerically construct axisymmetric, stationary spacetimes describing a black hole with a (synchronized) boson cloud. To that end, we solve the fully relativistic Einstein-Klein-Gordon and Einstein-Proca equations for scalar and vector boson clouds, respectively. These are, for a complex massive scalar field  $\Phi$  coupled to gravity,

$$G_{ab}/(8\pi) = \nabla_b \Phi^* \nabla_a \Phi + \nabla_a \Phi^* \nabla_b \Phi - g_{ab} (\mu^2 \Phi^* \Phi + \nabla_c \Phi \nabla^c \Phi^*), \quad (11)$$

$$\nabla_a \nabla^a \Phi = \mu^2 \Phi, \quad (12)$$

where  $G_{ab}$  is the Einstein tensor associated with the metric  $g_{ab}$ . For the case of a complex massive vector field  $A_b$  with associated field strength tensor

$$F_{ab} = \nabla_a A_b - \nabla_b A_a, \quad (13)$$

the Einstein-Proca equations are

$$G_{ab}/(8\pi) = \frac{1}{2} \mu^2 (A_b A_a^* + A_a A_b^*) - \frac{1}{2} \mu^2 A_c A^{*c} g_{ab} - \frac{1}{4} g_{ab} F_{cd}^* F^{cd} - \frac{1}{2} g^{cd} (F_{ac}^* F_{db} + F_{bc}^* F_{da}), \quad (14)$$

$$\nabla^a F_{ab} = \mu^2 A_b. \quad (15)$$

We do not consider any additional non-gravitational interactions. Imposing axisymmetry and stationarity of the metric, the spacetime exhibits the Killing vectors  $\varphi_a$  and  $t_a$ , respectively. This assumption implies that the Lie derivative of the scalar field along the Killing vector fields satisfies

$$\mathcal{L}_\varphi \Phi = im\Phi, \quad \mathcal{L}_t \Phi = -i\omega\Phi, \quad (16)$$

and similarly for the vector  $A_a$ . We further assume the synchronicity condition between the cloud frequency and the black hole horizon,  $\omega = m\Omega_H$ ; i.e., the bosonic fields saturate the black hole superradiance condition. In this study, we restrict to solutions corresponding to the end-point of the fastest growing superradiant unstable modes: we set  $m = 1$ .

Our general approach to numerically constructing these solutions is similar to Refs. [48–51], though the particular form for the metric ansatz that we use and some other details are different, and we give the full expressions for the elliptic equations that are solved in Appendix B. As in Refs. [48–51], we use a grid covering the angular domain and a compactified radial coordinate that goes from the black hole horizon to spatial infinity. We solve these discretized partial differential equations using an adapted version of Newton-Raphson method that was initially developed for boson star initial data in Ref. [57]. For more details on how these solutions are constructed, see Appendix B.

#### B. Covering the parameter space

We construct black hole-boson cloud solutions across the two dimensional parameter space labelled by the frequency  $\omega$  and the black hole radius (in units of the boson mass  $\mu$ ) by beginning from some seed solution and making small changes to these input quantities to relax to a nearby solution and then repeating. For each solution, we record the frequency  $\omega$ , the black hole mass  $M_{\text{BH}}$  and angular momentum  $J_{\text{BH}}$ , and the total boson cloud mass  $M_{\text{cloud}}$  and angular momentum  $J_{\text{cloud}}$  (see Appendix A for how these quantities are calculated). The two dimensional parameter space of solutions can alternatively be parameterized in terms of  $M_{\text{cloud}}/M_{\text{BH}}$  and  $\alpha$ . In terms of cloud mass, we cover the range going from a maximum of  $M_{\text{cloud}}/M_{\text{BH}} \approx 0.12$  down to small values of the cloud mass (as low as  $M_{\text{cloud}}/M_{\text{BH}} \approx 0.001$ , which can then be linearly extrapolated to zero). These encompass the cloud solutions that might arise through superradiance<sup>4</sup>. In terms of  $\alpha$ , we consider values ranging from the maximum allowed values for  $m = 1$  ( $\alpha \approx 0.5$  for scalars and

<sup>4</sup> We estimate whether a cloud could be formed around an isolated black hole via superradiance by checking whether the total angular momentum in the spacetime divided by the total mass squared is less than one. This gives that  $M_{\text{cloud}}/M_{\text{BH}} < 0.11$ .

$\alpha \approx 0.6$  for vectors), down to small values of  $\alpha$ , where the scales of this problem become disparate [recall, the black hole radius is  $\sim \alpha/\mu$ , while the cloud radius is  $\sim 1/(\alpha\mu)$ ], requiring more computational resources to resolve both objects. Due to this limitation, we include results for numerical solutions with  $\alpha > \alpha_{\min}$ , where  $\alpha_{\min} = 0.2$  in the scalar case and  $\alpha_{\min} = 0.09$  in the vector case. We reach a lower value of  $\alpha$  in the vector case because the fastest growing state is more compact than in the scalar case. In total, we compute  $\approx 6000$  solutions in the scalar case and  $\approx 13000$  solutions in the vector case.

We use these numerical solutions to interpolate and extrapolate over the whole physically relevant parameter space. First, a bivariate spline is used to interpolate over these solutions<sup>5</sup> and calculate the frequency on a regular grid of  $\alpha$  and  $M_{\text{cloud}}/M_{\text{BH}}$ . For each fixed value of  $\alpha$ , we then fit  $\omega$  to the best fit polynomial in cloud mass of the form

$$\frac{\omega}{\mu} = \sum_{q=0}^2 f_q(\alpha) \left( \frac{M_{\text{cloud}}}{M_{\text{BH}}} \right)^q, \quad (17)$$

where the choice to include only up to quadratic terms in cloud mass is motivated by the negligible contribution of higher order terms, as detailed in Appendix E2. Then the cloud mass-independent part of the frequency is described by  $f_0$ , and the frequency shift  $\Delta\omega = \omega - \omega(M_{\text{cloud}} = 0)$  is described by  $f_1$  and  $f_2$  for each value of  $\alpha$ . We compare  $f_0(\alpha)$  with test field results and find good agreement (see Appendix E for details). Then we interpolate<sup>6</sup>  $f_q(\alpha)$  over  $\alpha$  to return a smooth function that can be evaluated at any  $\alpha$ .

Extrapolation of these relativistic results to lower values of  $\alpha < \alpha_{\min}$  is done by leveraging the non-relativistic results reviewed in Sec. IIB. We fit the difference in the coefficients in Eq. (17) from their non-relativistic limit with a higher order polynomials of the form

$$\begin{aligned} f_1(\alpha) + C_{\text{nr}}\alpha^2 &= \sum_{p=3}^6 c_{p,1}\alpha^p, \\ f_2(\alpha) &= \sum_{p=3}^6 c_{p,2}\alpha^p, \end{aligned} \quad (18)$$

where  $C_{\text{nr}}$  is calculated from the non-relativistic limit (see Sec. IIB), with  $C_{\text{nr}} = 93/512$  in the scalar case and  $C_{\text{nr}} = 5/8$  in the vector case. We fit for  $c_{p,q}$  using points in the low  $\alpha$  regime<sup>7</sup> and extrapolate to lower values to

estimate the relativistic correction there. We find that the fit parameters in Eq. (18) are order unity or smaller, guaranteeing that the fit will approach the expected non-relativistic limit at small  $\alpha$ .

## IV. RESULTS

### A. Frequency Shift

We begin by comparing the relativistic frequency shift for scalar and vector boson clouds calculated in this work to the non-relativistic approximation described in Sec. IIB. In Fig. 1, we plot the quantity  $d\omega/dM_{\text{cloud}}$  at  $M_{\text{cloud}} = 0$ , which means taking only the part of the frequency shift linear in cloud mass and ignoring any higher order parts. (As shown in Appendix E2, the quadratic in cloud mass term in the relativistic case contributes at the percent level.) From the plot, it is apparent that the deviation of the relativistic calculation from the non-relativistic limit can be as large as 40 – 50% in the scalar case and 70 – 80% in the vector case.

In Fig. 1, we also compare our results to the quasi-relativistic calculation of the frequency shift used in Ref. [45], which is computed using the energy density computed from the relativistic test field, but still utilizing the Newtonian expression for the frequency shift in terms of this quantity. We find that the test field calculation does well in the scalar case up to moderately high values of  $\alpha$ , significantly improving over the non-relativistic expression up until  $\alpha \approx 0.35$ . However, for  $\alpha > 0.37$  the test field calculation actually becomes less accurate than the leading order non-relativistic limit<sup>8</sup>. In the vector case, the test field calculation always performs worse than the non-relativistic limit. It seems that in this case including only some relativistic corrections can actually give a worse result than the purely non-relativistic one, though there may be a more accurate way to generalize the Newtonian expression for the frequency shift to the relativistic regime.

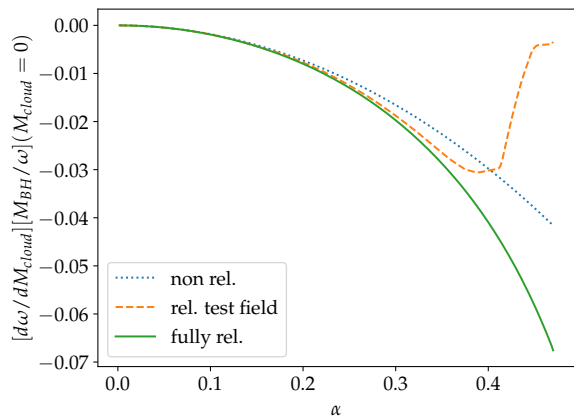
We next comment on the estimated errors in the fully relativistic calculation of the frequency shift. As described in Appendix C, we use a combination of numerical error due to finite resolution, theoretical error due to our oscillation-averaged approximation, and interpolation error due to the finite number of numerical points to estimate a total error in the evaluation of the frequency shift. A summary of these different error estimates can be found at the beginning of Appendix C. As can be seen there, in the scalar case, the relative error in the frequency shift ranges from a few times 0.1% to 1% across the parameter space, and is dominated by the

<sup>5</sup> We use a fifth order bivariate spline interpolation algorithm from `scipy`.

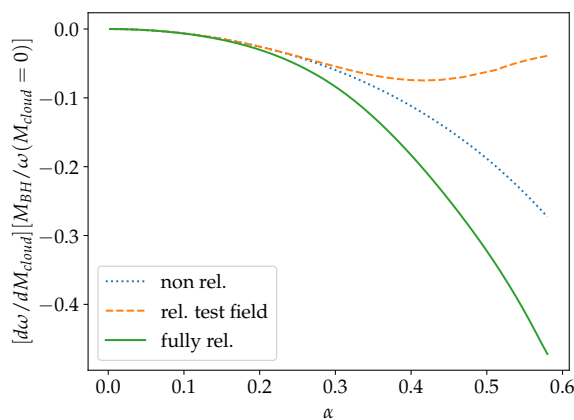
<sup>6</sup> Here we use a cubic spline interpolating algorithm from `scipy`.

<sup>7</sup> We use points with  $\alpha < 0.3$  in the scalar case and  $\alpha < 0.15$  in the vector case.

<sup>8</sup> In Fig. 6 of Ref. [45], there is a plotting error in the test field calculation shown due to the use of an expression for the black hole spin that is inaccurate for high spin or high  $\alpha$ .



(a) Scalar field



(b) Vector field

Figure 1: The cloud mass dependence of the frequency of oscillation of the cloud around the black hole for scalar bosons (top) and vector bosons (bottom). The leading order non-relativistic result ( $\propto \alpha^3$ ) is plotted along with the relativistic test field result from Ref. [45] and the fully relativistic result of this paper.

interpolation error. For the vector case, on the other hand, the theoretical error is larger, and dominates over the numerical error and the interpolation error in much of the parameter space. The relative error in the vector frequency shift ranges from 0.001% at low  $\alpha$  to 1% at the highest values of  $\alpha$  considered.

## B. Implications for gravitational wave searches for ultralight bosons

The more accurate relativistic frequency shift calculations described in the previous section can be used to better model the frequency evolution of the gravitational wave signal from an oscillating boson cloud. We have incorporated these results into SuperRad, a waveform

model for superradiant clouds described in Ref. [45]. In Fig. 2, we plot example waveforms for scalar and vector boson cases for an initial black hole with properties consistent with the remnant from the binary black hole merger GW200308 [58]. Here we can see the enhanced frequency shift in the fully relativistic calculation compared to the non-relativistic estimate, corresponding to a larger change in frequency and a stronger chirp as the cloud dissipates through gravitational radiation.

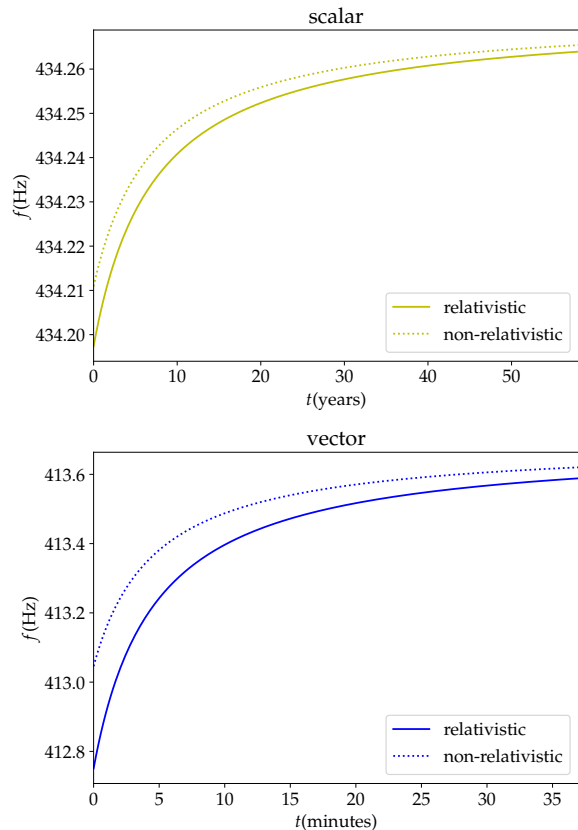


Figure 2: The frequency evolution for an example waveform with an initial black hole of dimensionless spin  $\chi_{\text{BH}} = 0.91$  and mass  $M_{\text{BH}} = 47 M_{\odot}$ , and an ultralight boson with mass  $m_b = 9.1 \times 10^{-13}$  eV (corresponding to  $\alpha = 0.32$ ). Here  $f$  is the gravitational wave frequency, plotted from the maximum cloud mass of  $M_{\text{cloud}}/M_{\text{BH}} \approx 3\%$  (5%) to the point where  $M_{\text{cloud}}/M_{\text{BH}} \approx 0.3\%$  (0.5%) for the scalar (vector) case.

We roughly estimate the phase error over one gravitational wave emission timescale with the relativistic calculation of the frequency shift, using the estimated relative error  $\delta\omega/\Delta\omega$ , as described in Appendix C. Recalling that the gravitational wave frequency is given by twice the oscillation frequency of the cloud, the additional gravitational wave phase offset due to the frequency shift is

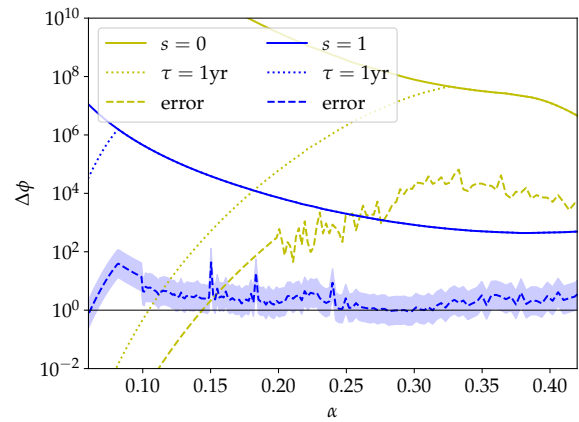
$$\Delta\phi = 2 \int_0^{\tau_{\text{GW}}} dt [\omega(t) - \omega(0)], \quad (19)$$

where here the time  $t = 0$  corresponds the end of the superradiant instability phase and the peak of the signal, before the cloud starts dissipating, and  $\tau_{\text{GW}}$  is the gravitational wave emission timescale. We translate our estimate of the error in the frequency shift into an estimate of the phase error in the updated waveform using

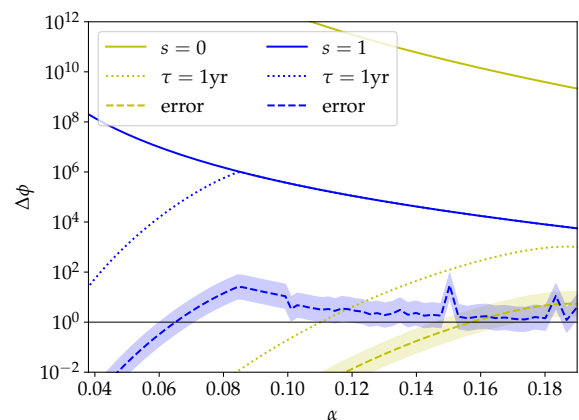
$$E(\Delta\phi) = 2 \int_0^{\tau_{\text{GW}}} dt \delta\omega \approx \Delta\phi \left( \frac{\delta\omega}{\Delta\omega} \right)_{t=0}. \quad (20)$$

The accumulated phase offset  $\Delta\phi$  for scalar and vector clouds with different values of  $\alpha$ , as well as the estimated error in this quantity, is shown in Fig. 3. We include both a case where the initial black hole is rapidly spinning, to illustrate the behavior at high values of  $\alpha$ , as well as a case with a more moderate spin typical of the remnant of a comparable mass binary black hole merger. The figure illustrates that, except for scalar bosons and low values  $\alpha$ , where the gravitational wave signal does not evolve significantly over the maximum one year period considered, this phase offset is significant, and the changing frequency needs to be taken into account. For the relativistically-correct frequency shift calculated here, we estimate that the theoretical error in much of the parameter space for vector bosons is on the order of a few radians over the characteristic timescale of the gravitational wave signal. This is nearing the regime where theoretical modelling errors would no longer be an impediment to coherent gravitational wave searches, although there are other reasons that such searches may not be practical, including uncertainty in black hole parameters and computational expense.

In addition to the ground based detector sources discussed above, we consider an example relevant for LISA in Fig. 4. Constituents of massive black hole binaries are expected to have higher dimensionless spins than stellar-mass black holes, and may also be promising candidates for binary follow-up searches for gravitational wave from vector clouds around merger remnants [45]. Following Ref. [59], when the phase error is the dominant source of error, a model with a maximum phase error of order  $1/\rho_{\text{max}}$  is sufficiently accurate for a signal with maximum signal-to-noise ratio (SNR) of  $\rho_{\text{max}}$ . In Fig. 4, we plot the phase error for the vector case using two different models. One model uses the relativistic frequency shift calculated in this work, and other uses the leading order non-relativistic frequency shift. The phase error corresponding to sufficiently accurate model for a signal with  $\rho_{\text{max}} = 10$  is approximately  $1/\rho_{\text{max}} = 0.1$ . From the plot, it can be seen that while the non-relativistic shift model is sufficient for  $\alpha < 0.115$  when  $\rho_{\text{max}} = 10$ , the relativistic shift model covers the larger range of  $\alpha < 0.18$ . It is evident that the improved waveform model is preferred for  $0.115 < \alpha < 0.18$  or for higher SNR signals at lower  $\alpha$ .



(a) Initial black hole with dimensionless spin  $\chi_{\text{BH}} = 0.99$ .



(b) Initial black hole with dimensionless spin  $\chi_{\text{BH}} = 0.7$ .

Figure 3: The phase offset after integrating the gravitational wave signal over its emission timescale, or one year if the gravitational wave timescale is longer than that. In each case the initial black hole mass is  $M_{\text{BH}} = 50 M_{\odot}$ . The jump in error at low  $\alpha$  is where the relativistic shift calculation is extrapolated. The shaded region around the error in phase offset corresponds to an uncertainty in the error of a factor of three, indicating that the error shown here is an order of magnitude estimate.

### C. Geometry

In addition to changing the oscillation frequency, the boson cloud will change the spacetime geometry around the black hole, which we can characterize using the solutions we construct. Here, we focus on calculating the change in the light ring and the ISCO of the black hole in the presence of a boson cloud, as these are related to how observations of accreting black holes are used to measure the black hole spin. There has been significant work on this topic in the past. A full null ray-tracing analysis was carried out for black holes with vector bo-

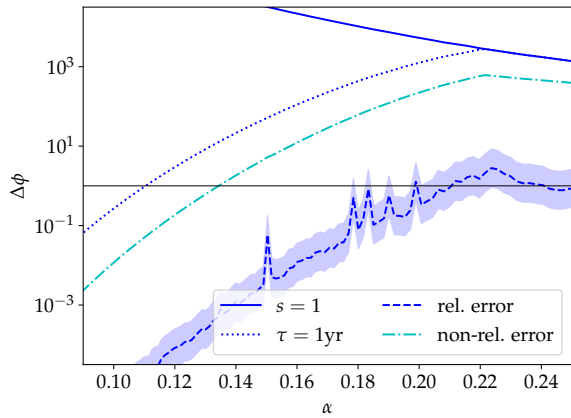


Figure 4: The phase offset after integrating the gravitational wave signal over its emission timescale, or one year if the gravitational wave timescale is longer than that. Here we consider a LISA source, with initial black hole mass  $M_{\text{BH}} = 5 \times 10^5 M_{\odot}$  and initial dimensionless spin  $\chi = 0.85$ . We compare the total accumulated phase, the error in the relativistic waveform, and the error in a waveform using the leading order non-relativistic frequency shift.

son clouds in Ref. [53], ISCO frequencies were calculated for black holes with scalar hair in Ref. [49], and predictions for  $K\alpha$  emission lines have been calculated using null-ray-tracing in Ref. [52] for black holes with scalar hair. Here, we calculate equatorial null and test particle orbits around black holes with both scalar and vector clouds.

For all the black hole-cloud solutions we construct, we calculate the position of the equatorial light ring and ISCO around a black hole in the presence of a super-radiant cloud as is described in Appendix D, using the circumferential radius to record our measured radii in a coordinate independent way. We compare the light ring and ISCO radii of a black hole with a scalar or vector cloud with those of a Kerr black hole with either the same black hole parameters (measured using the horizon quantities) or the same total mass and angular momentum (in particular we use the ADM mass [60]). The results for the deviation of the light ring from the Kerr values are shown in Fig. 5 and the results for the ISCO radius are shown in Fig. 6. As one might expect, the biggest effect comes from the comparison where the global quantities are kept fixed, due to the significant amount of mass and angular momentum that can be carried in the cloud. However, for the vector case at high  $\alpha$ , the cloud can have non-negligible effect on the near horizon geometry, shifting the light ring and ISCO radius by up to a few percent.

In addition to calculating the location of the ISCO for the black hole-boson cloud systems, we calculate the ISCO frequency, and the redshift of light emitted by an

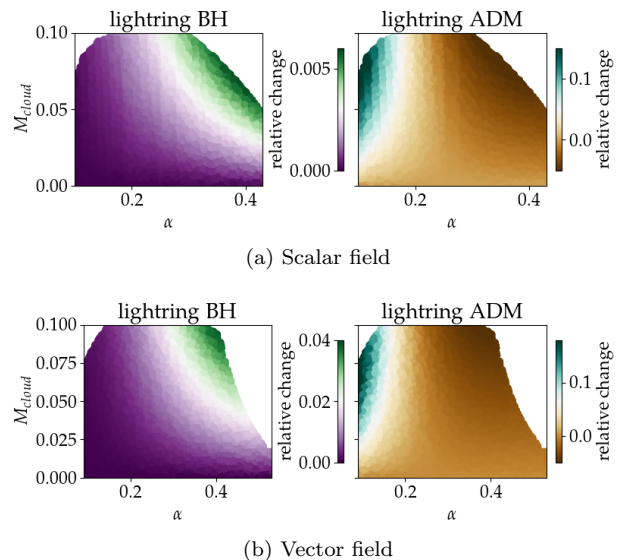


Figure 5: The relative difference in the circumferential radius of the light ring for a black hole with a boson cloud compared to a Kerr black hole with the same black hole mass and spin (left panels) or the same global mass and angular momentum (right panels).

observer traveling along the ISCO as measured by another observer at rest at infinity. In particular, we calculate the redshift for a light ray emitted tangent to the observer's trajectory in the same direction (prograde to the black hole's spin), which we call  $z_{\text{ISCO}}$ , and show the deviation in this quantity from its Kerr value in Fig. 6, either fixing the black hole or the global mass and angular momentum. This shows similar behavior to the ISCO radius. We comment on how the deviations in these quantities from their Kerr values might be related to spin mis-measurement in the presence of a boson cloud in the next section.

The numerical values for the light ring radius, ISCO radius, frequency, and redshift (for light emitted both in the same or opposite direction as the emitter orbiting at the ISCO) of black holes with scalar and vector boson clouds are publically available<sup>9</sup>.

#### D. Implications for Kerr parameter measurements

One method for inferring black hole spins is to measure how the emission from accreting black holes is redshifted (or blue shifted) [61–63]. Roughly speaking, the maximum redshift is taken to come from the ISCO since any material inside the ISCO is not expected to contribute to the observed electromagnetic spectrum under the assumption that the accretion disk is thin and oriented on

<sup>9</sup> Data files with the geometric quantities and usage examples can be found at <https://www.bitbucket.org/weast/superrad>.



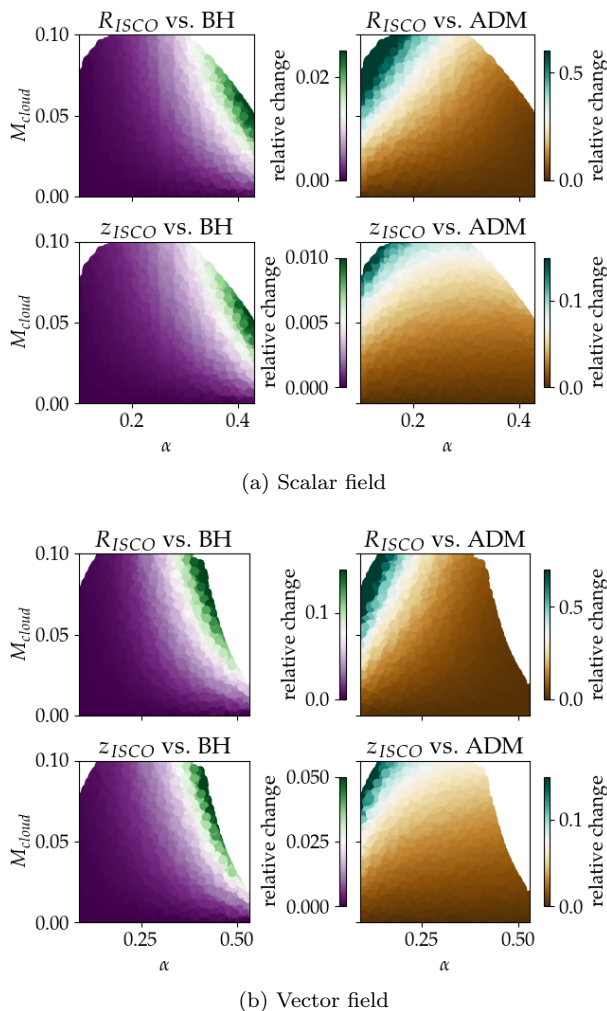


Figure 6: Here we show the ISCO radius and the redshift from the ISCO to infinity in the presence of a boson cloud, compared to the ISCO radius and redshift from the ISCO of a Kerr black hole with either the same central black hole’s properties or the same global mass and angular momentum. The quantity plotted is the relative difference in  $\omega_1$  and  $\omega_2$  where  $\omega_1$  is the frequency measured by the observer traveling along the ISCO and  $\omega_2$  is the frequency measured by a stationary observer at infinite distance. The result plotted here is for light emitted tangent to the observer’s motion on the ISCO and in the same (prograde) direction.

the equator. Since the presence of a cloud can affect the position and redshift at the ISCO, we wish to estimate how much it would affect these spin measurements.

There are two main methods for measuring black hole spins from spectra,  $K\alpha$  line broadening and continuum fitting. The  $K\alpha$  line broadening method yields a dimensionless redshift measurement that can be used to directly fit the dimensionless spin [62]. The continuum fitting method gives a dimensionful ISCO radius measurement that must then be scaled by an independent

mass measurement, often from distant orbiting dynamics [61]. A mass measurement using distant orbiting dynamics would give a value close to the total mass (e.g. in a black hole-cloud system), rather than the central black hole mass.

A complete analysis of how the presence of a boson cloud would affect an accreting black hole would require solving for accretion disk profiles on the black hole-cloud solutions and tracing out the emission that they source, which is beyond the scope of this work. We further note that we here we are restricting to our axisymmetric and stationary spacetimes, and neglecting the effect of an oscillating component to the gravitational potential that would be present in the case of single (real) scalar or vector field (see, e.g., Ref. [64]). However, as a rough estimate of the discrepancy between the dimensionless spin  $\chi = J_{\text{BH}}/M_{\text{BH}}^2$  one would infer from such methods when assuming a Kerr black hole when a boson cloud is present, we consider how the value of  $z_{\text{ISCO}}$ , or the ratio  $R_{\text{ISCO}}/M_{\text{ADM}}$ , maps to a dimensionless black hole spin assuming Kerr. We define the difference between this estimated black hole spin  $\chi_{\text{est.}}$  and the true dimensionless spin  $\chi$  of a black hole surrounded by a boson cloud as

$$\Delta\chi = \chi_{\text{est.}} - \chi. \quad (21)$$

We plot  $\Delta\chi$  in Fig. 7 for the both the case where one combines the dimensionful ISCO radius with the global mass (left panels), and the case based on the dimensionless redshift  $z_{\text{ISCO}}$  (right panels). When considering  $R_{\text{ISCO}}/M_{\text{ADM}}$ , both the scalar and boson case show a similar overestimate in the dimensionless spin up to moderately high values, that is mostly just due to the overestimate of the black hole mass. Interestingly, for the most relativistic vector boson cases, the effect on the geometry near the black hole becomes significant, and causes this quantity to give an underestimate of the black hole spin. Using the redshift at the ISCO has a smaller effect, leading to a maximum overestimate in the dimensionless spin of  $\sim 1\%$  in the scalar case, and  $5\%$  in the vector case.

## V. DISCUSSION AND CONCLUSION

In this work, we have used fully general relativistic solutions to study the self-gravity effects of boson clouds that might form around black holes through the superradiant instability. In particular, we have focused on how the frequency of the cloud’s oscillation changes due to the non-vanishing mass of the cloud. This impacts the frequency shift and evolution of the gravitational waves emitted by the clouds. We found that relativistic effects can enhance this frequency shift by up to a factor of two over non-relativistic estimates obtained previously. Further, our current fully relativistic computation of the frequency shift is accurate up to uncertainties at the percent level or better. The remaining errors are due both to finite numerical resolution, as well as theoretical error

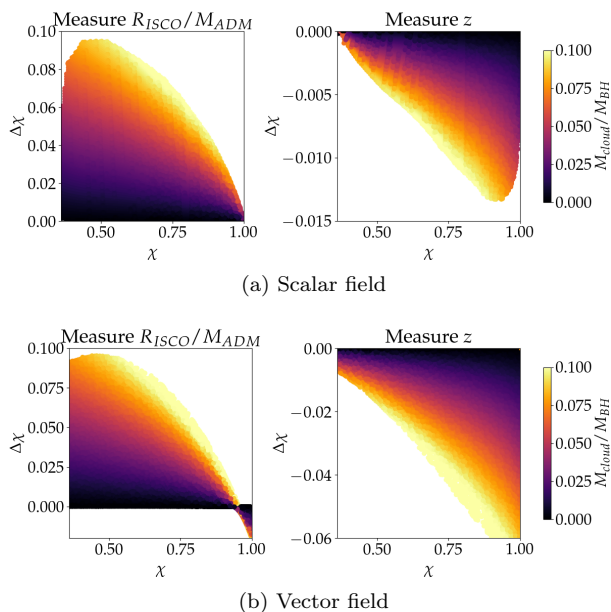


Figure 7: The effect of the presence of a boson cloud on the dimensionless spin measurements using a known mass and redshift measurements. The results shown are only for clouds that could be formed through superradiance around an isolated black hole. The spin shown here is the spin of the central black hole after the cloud’s formation.

arising from an oscillation-average approximation taken here.

Using this fully relativistic frequency shift, we improved the gravitational waveform model **SuperRad** [45]. This allows for accurate modeling of the loudest, and thus fastest evolving, boson cloud gravitational wave signals (i.e., those where the change in frequency during the observation time is most significant). This is particularly relevant for targeting gravitational wave emitted by ultralight vector boson clouds around binary black hole remnants. Currently, proposed searches for such signals are based on semi-coherent search methods, which are fast and more robust to modelling errors, at the expense of have a reduced sensitivity compared to a fully coherent searches [43]. The results here can be used to better tune the parameters of such searches, but may also be leveraged to design more sensitive search techniques. This is relevant not only for current ground-based gravitational wave detectors, but also for supermassive black hole mergers and space-based detectors such as LISA.

Most previous continuous wave searches for signals from boson clouds have focused on scalar bosons in the small  $\alpha$  regime (for example, in Ref. [31] the largest value of  $\alpha$  considered is  $\alpha = 0.15$ ) and often use frequency binning methods that assume the frequency variation within a timestep (or a minimum coherence time) is below a given threshold. In these cases, the relativistic correction to the rate of frequency evolution, and therefore

the correction to the maximum  $\alpha$  constrained, is at the level of only a few percent. However, for larger values of  $\alpha$ , this correction will be more significant. For example, Ref. [39] estimated the detectability of scalar boson clouds with  $\alpha \leq 0.5$  for blind searches, and Ref. [43] estimated the detectability of targeted searches for vector boson clouds with  $\alpha \lesssim 0.2$ . Considering the typical remnant of a comparable mass, low-spin binary black hole merger, the strain is maximized for  $\alpha \approx 0.17$ , where the relativistic frequency shift correction is  $\approx 10\%$  in the vector boson case.

In this work, we have not considered bosonic fields with non-gravitational self-interactions or interactions with other fields, which may give rise to additional radiation channels or affect the saturation the superradiant instability and the expected gravitational wave signal [44, 65–72]. For future work, it would be interesting to see whether relativistic black hole-boson cloud solutions like those considered here can be used to incorporate the impact of these interactions on the observational signatures (see, e.g., Ref. [73]).

Finally, we have also studied how the boson cloud will change the black hole spacetime, and commented on how this may affect spin measurements based on observations of accreting black holes. As is discussed in Ref. [74], since the two main methods of spin measurement from redshifts, continuum fitting and  $K\alpha$  line broadening, give different biases in the presence of a boson cloud, the difference between the values of these two measurements can be used to probe the existence of extra matter located close to the black hole. As was assumed in Ref. [74], we find here that the discrepancy in the spin from mapping the dimensionless redshift to its value in an isolated black hole is subdominant to the discrepancy due to the use of the dimensionful ISCO measurement in the scalar case. In the vector case, however, the former can be more significant at moderately high spin due to the stronger effect on the geometry in the vicinity of the black hole horizon, potentially giving rise to a more sensitive probe for the presence of a boson cloud.

## VI. ACKNOWLEDGEMENTS

The authors would like to thank Dana Jones and Ling Sun for helpful discussions. W.E. and T.M. acknowledge support from a Natural Sciences and Engineering Research Council of Canada Discovery Grant and an Ontario Ministry of Colleges and Universities Early Researcher Award. This research was supported in part by Perimeter Institute for Theoretical Physics. Research at Perimeter Institute is supported in part by the Government of Canada through the Department of Innovation, Science and Economic Development and by the Province of Ontario through the Ministry of Colleges and Universities. This research was enabled in part by support provided by SciNet (www.scinethpc.ca) and the Digital Research Alliance of Canada (alliancecan.ca). Calculations

were performed on the Symmetry cluster at Perimeter Institute, the Niagara cluster at the University of Toronto, and the Narval cluster at Ecole de technologie supérieure in Montreal.

## Appendix A: Physical quantities

For the black hole-boson cloud solutions constructed in this work, we calculate several quantities that characterize the mass and angular momentum associated with the black hole and the cloud. To calculate the boson cloud mass, we use the Komar mass integral, as is done in Refs. [49–51], with

$$M_{\text{cloud}} = - \int_{\Sigma} dS_a (2T_b^a t^b - T t^a), \quad (\text{A1})$$

where  $T_{ab}$  is the stress energy tensor with trace  $T$ , the integral is over a space-like hypersurface  $\Sigma$ , with  $dS_a = n_a dV$  proportional to the unit future pointing normal  $n_a$  to that hypersurface, and  $t^b$  is the Killing vector associated with the stationary spacetime. The cloud angular momentum  $J_{\text{cloud}}$  is calculated using the Komar integral as in the cloud mass integral in Eq. (A1), but with  $t^a$  replaced by the azimuthal Killing vector  $\varphi^a$ . For both these quantities, we use a special treatment of the inner boundary, to avoid error due to setting the inner radial boundary slightly off the black hole horizon. This involves interpolating the integrand over the last few points before the horizon point then extrapolating to the point on the horizon. We use a linear interpolation because the extrapolated point converges well in that case.

We calculate the black hole mass using two different approaches. We can either calculate the ADM mass and subtract the cloud mass or directly calculate the horizon mass. In different regimes, these two calculations have better associated error and so we calculate both in order to minimize error as well as to check our mass and angular momentum calculations are consistent. The ADM mass and total angular momentum  $J$  can be calculated using the asymptotic behaviour of the metric as is described in Ref. [49] (Eq. 3.15). We also calculate the horizon mass as is described in Ref. [49] using the expression

$$M_{\text{BH}} = 2T_H S + 2\Omega_H (J - J_{\text{cloud}}), \quad (\text{A2})$$

where the Hawking temperature  $T_H$ , and the entropy  $S$  are calculated according to Ref. [49].

In the scalar case, we use the horizon mass and the Komar cloud mass in all of the parameter space and in the vector case, we use the ADM mass and the Komar cloud mass for high  $\alpha$  and the horizon mass and the Komar cloud mass for lower  $\alpha$ . In each case, we check that these two definitions give results that are consistent within the numerical error.

## Appendix B: Constructing solutions

### 1. Elliptic differential equations

We formulate differential equations using the Einstein-Klein Gordon and Einstein-Proca equations (along with a Lorenz condition in the Proca case). The solution is then constructed from an ansatz. We use metric ansatz with an explicit horizon in the Lewis-Papapetrou coordinates:

$$ds^2 = -fNdt^2 + \frac{l}{f} \left[ g \left( \frac{dr^2}{N} + r^2 d\theta^2 \right) + r^2 \sin^2 \theta \left( d\varphi - \frac{\omega_m}{r} dt \right)^2 \right], \quad (\text{B1})$$

where  $N = (r - r_H)/r$  vanishes at the horizon radius. This ansatz is stationary and axisymmetric, and so the metric functions  $f$ ,  $l$ ,  $g$ , and  $\omega_m$  are real valued functions of only two coordinates ( $r$  and  $\theta$ ) and can be solved on a two dimensional grid. Due to the equatorial symmetry, we can restrict the angular domain to the region above the equatorial plane,  $\theta \in (0, \pi/2)$ . We use a compactified radial coordinate  $x = (r - r_H)/r$ , and include slight offsets from the boundaries of  $0 < x < 1$  and  $0 < \theta < \pi/2$  such that our numerical grid boundaries are at  $10^{-7} < x < 1 - 10^{-7}$  and  $10^{-7} < \theta < \pi/2 - 10^{-7}$ . The matter field values are solved simultaneously on the same grid. The scalar field ansatz is

$$\Phi(t, r, \theta, \varphi) = \phi(r, \theta) e^{-i\omega t + im\varphi}. \quad (\text{B2})$$

Here  $\phi(r, \theta)$  is a real valued function,  $m \in \mathbb{Z}$ , and  $\omega \in \mathbb{R}$ . The function  $\phi$  is solved along with the metric functions in  $r$ - $\theta$  space to give a full solution. In the vector case we use the ansatz:

$$A_0(t, r, \theta, \varphi) = iV(r, \theta) e^{-i\omega t + im\varphi} \quad (\text{B3})$$

$$A_r(t, r, \theta, \varphi) = H_1(r, \theta) e^{-i\omega t + im\varphi} \quad (\text{B4})$$

$$A_\theta(t, r, \theta, \varphi) = H_2(r, \theta) e^{-i\omega t + im\varphi} \quad (\text{B5})$$

$$A_\varphi(t, r, \theta, \varphi) = i \sin(\theta) H_3(r, \theta) e^{-i\omega t + im\varphi} \quad (\text{B6})$$

and solve for real valued functions  $V(r, \theta)$ ,  $H_1(r, \theta)$ ,  $H_2(r, \theta)$ , and  $H_3(r, \theta)$ . The choice of  $\omega$  and  $r_H$  (in units of  $\mu$ ) determines the solution.

We formulate the scalar (vector) equations of motion by combining Einstein's equation with the Klein Gordon (Proca and Lorentz) equation(s). We get a set of five (eight) second order differential equations, such that we have:

$$\partial^2 F_i = \text{Polynomial}(\partial F_j, F_j) \quad (\text{B7})$$

for each real valued field  $F_i$ . We use a metric ansatz that is different from Refs. [48–51], and we find that, while this ansatz is well behaved in the boson star case, there is a numerical divergence at the horizon in the black hole with boson cloud case. We remove that divergence by including an overall factor of  $x^3$  in all the equations of

motion given below. We list the equations of motion for a complex vector field in the presence of a black hole

here, these expressions are also available in a notebook accompanying this article. They are

$$\begin{aligned}
\partial_r^2 V + \partial_\theta^2 V / (r(r-r_H)) = & - \left( (r_H - r) \sin(\theta) \left( -\csc(\theta) \partial_r l \partial_r V r^3 - 2\omega_m \partial_r H_3 \partial_r l r^2 - 2l \partial_r H_3 \partial_r \omega_m r^2 - 4 \csc(\theta) l \partial_r V r^2 \right. \right. \\
& + r_H \csc(\theta) \partial_r l \partial_r V r^2 + 2m^2 \csc^3(\theta) g l V r - 2 \cot(\theta) \csc(\theta) l \partial_\theta V r - \csc(\theta) \partial_\theta l \partial_\theta V r - 2l \omega_m \partial_r H_3 r + 2r_H \omega_m \partial_r H_3 \partial_r l r \\
& + 2r_H l \partial_r H_3 \partial_r \omega_m r + 4r_H \csc(\theta) l \partial_r V r - 4 \cot^2(\theta) H_3 l \omega_m - 4 \cot(\theta) l \omega_m \partial_\theta H_3 - 2 \cot(\theta) H_3 \omega_m \partial_\theta l \\
& - 2\omega_m \partial_\theta H_3 \partial_\theta l - 2 \cot(\theta) H_3 l \partial_\theta \omega_m - 2l \partial_\theta H_3 \partial_\theta \omega_m + 2m \csc(\theta) H_2 (\omega_m \partial_\theta l + l (2 \cot(\theta) \omega_m + \partial_\theta \omega_m)) \\
& \left. \left. + 4r_H l \omega_m \partial_r H_3 - 2 \csc(\theta) H_1 (mr(r_H - r) \omega_m \partial_r l + l (-rr_H \omega + m(2r_H - r) \omega_m + mr(r_H - r) \partial_r \omega_m)) \right) \right) \\
f^2 + 2(r_H - r)l \left( \mu^2 g l V r^3 + \omega H_1 \partial_r f r^3 + \partial_r f \partial_r V r^3 - r_H \omega H_1 \partial_r f r^2 - 2m H_1 \omega_m \partial_r f r^2 + 2\omega_m \sin(\theta) \partial_r f \partial_r H_3 r^2 \right. \\
& - r_H \partial_r f \partial_r V r^2 + \partial_\theta f \partial_\theta V r + 2mr_H H_1 \omega_m \partial_r f r - 2r_H \omega_m \sin(\theta) \partial_r f \partial_r H_3 r + 2 \cos(\theta) H_3 \omega_m \partial_\theta f - H_2 (-r\omega + 2m\omega_m) \partial_\theta f \\
& + 2\omega_m \sin(\theta) \partial_\theta f \partial_\theta H_3 \left. \right) f + 2rl^2 (rgV(-r\omega + m\omega_m)^2 - (r_H - r) H_1 \omega_m \sin^2(\theta) (\omega_m - r \partial_r \omega_m) (-r\omega + m\omega_m) \\
& + \omega_m \sin^2(\theta) (\partial_r \omega_m \partial_r V r^3 + \omega_m \sin(\theta) \partial_r H_3 \partial_r \omega_m r^2 - \omega_m \partial_r V r^2 - r_H \partial_r \omega_m \partial_r V r^2 + \partial_\theta \omega_m \partial_\theta V r - \omega_m^2 \sin(\theta) \partial_r H_3 r \\
& - r_H \omega_m \sin(\theta) \partial_r H_3 \partial_r \omega_m r + r_H \omega_m \partial_r V r + \cos(\theta) H_3 \omega_m \partial_\theta \omega_m - H_2 (-r\omega + m\omega_m) \partial_\theta \omega_m + \omega_m \sin(\theta) \partial_\theta H_3 \\
& \left. \partial_\theta \omega_m + r_H \omega_m^2 \sin(\theta) \partial_r H_3 \right) \left( 2r^2 (r_H - r)^2 f^2 l \right)^{-1}, \tag{B8}
\end{aligned}$$

$$\begin{aligned}
\partial_r^2 H_1 + \frac{\partial_\theta^2 H_1}{r(r-r_H)} = & \left( \frac{2 \cot(\theta) (r_H - r) \partial_\theta H_1}{r} - \frac{4(r_H - r) \partial_\theta H_2}{r^2} \right. \\
& + \frac{2gl(m\omega_m - \omega r)(H_3 \omega_m \sin(\theta + rV(r, \theta)) \partial_r f}{f^3} + 4(r_H - r) \partial_r H_1 - \frac{2(r_H - r) \partial_\theta g (\partial_\theta H_1 - \partial_r H_2)}{gr} \\
& - \frac{(r_H - r) \partial_\theta l (\partial_\theta H_1 - \partial_r H_2)}{lr} + \frac{(r_H - r) \partial_\theta l \partial_r H_2}{lr} - \frac{2(r_H - r) (\mu^2 g H_1 l r^2 + \partial_\theta f (\partial_r H_2 - \partial_\theta H_1))}{fr} \\
& - \frac{2m \csc(\theta) g (r_H - r) (m \csc(\theta) H_1 - \partial_r H_3)}{r} + \frac{(r_H - r) ((r_H - r) r \partial_r H_1 - 2 \partial_\theta H_2) \partial_r l}{lr} \\
& + \frac{2m \csc(\theta) g (r_H - r) (H_3 (2l + r \partial_r l) - lr \partial_r H_3)}{lr^2} - ((r_H - r) \partial_r f (-H_2 (2 \cot(\theta) l + \partial_\theta l) + 2l (m \csc(\theta) g H_3 \\
& - \partial_\theta H_2 + (r_H - r) r \partial_r H_1) + H_1 (2l(r_H - 2r) + (r_H - r) r \partial_r l)) (flr)^{-1} \\
& + \frac{(r_H - r) \partial_r g (-H_2 (2 \cot(\theta) l + \partial_\theta l) - 2l (\partial_\theta H_2 + r(r - r_H) \partial_r H_1) + H_1 (2l(r_H - 2r) + (r_H - r) r \partial_r l))}{glr} \\
& - \frac{2gl(m\omega_m - \omega r) (H_1 (m\omega_m - \omega r) - \omega_m \sin(\theta) \partial_r H_3 - r \partial_r V)}{f^2} \\
& - (2gl (H_3 \sin(\theta) (m(r_H - 2r) \omega_m^2 - r (-\omega r + 2m(r_H - r) \partial_r \omega_m) \omega_m - \omega r^2 (r - r_H) \partial_r \omega_m) \\
& + r (-rV(r, \theta) (-r_H \omega + m\omega_m + m(r_H - r) \partial_r \omega_m) - (r_H - r) (m\omega_m - \omega r) (\omega_m \sin(\theta) \partial_r H_3 + r \partial_r V))) \\
& \left. (f^2 r (r - r_H))^{-1} - \frac{H_2 (r_H - r) (4 \cot(\theta) l^2 + (2 \partial_\theta l + 2 \cot(\theta) r \partial_r l - r \partial_r \partial_\theta l) l + 2r \partial_\theta l \partial_r l)}{l^2 r^2} \right) \\
& + \frac{H_1 (r_H - r) (4(r_H - r) l^2 + r ((3r_H - 4r) \partial_r l + r(r - r_H) \partial_r^2 l) l + 2(r_H - r) r^2 (\partial_r l)^2)}{l^2 r^2} \left. \right) (2(r_H - r)^2)^{-1}, \tag{B9}
\end{aligned}$$

$$\begin{aligned}
\partial_r^2 H_2 = & \left( \frac{2(r_H - r) ((r_H - r) \partial_r f (\partial_\theta H_1 - \partial_r H_2) - \mu^2 r g H_2 l)}{f} \right. \\
& - \frac{2gl(m\omega_m - \omega r) (H_2 (m\omega_m - \omega r) - \sin(\theta) \partial_\theta H_3 \omega_m - \cos(\theta) H_3 \omega_m - r \partial_\theta V)}{f^2} \\
& + ((r_H - r) (-2r(r_H - r) \partial_r gl (\partial_\theta H_1 - \partial_r H_2) + g (-r(r_H - r) \partial_r l (\partial_\theta H_1 - \partial_r H_2) - 2l (r_H \partial_\theta H_1 \\
& + r(r - r_H) \partial_r \partial_\theta H_1 - r_H \partial_r H_2)) + 2m \csc^2(\theta) g^2 l (-m H_2 + \sin(\theta) \partial_\theta H_3 + \cos(\theta) H_3)) (rgl) \left. \right) (2(r_H - r)^2)^{-1} \tag{B10}
\end{aligned}$$

$$\begin{aligned}
\partial_r^2 H_3 + \partial_\theta^2 H_3 / (r(r-r_H)) &= (4(r_H-r)fl(-mr^2 \csc(\theta)\partial_r f H_1 + mrr_H \csc(\theta)\partial_r f H_1 - m \csc(\theta)\partial_\theta f H_2 + r^2 \partial_r f \partial_r H_3 \\
&+ \partial_\theta f \partial_\theta H_3 - rr_H \partial_r f \partial_r H_3 + \cot(\theta)\partial_\theta f H_3 - \mu^2 r^2 g H_3 l) - (\csc^2(\theta)(r_H-r)f^2(H_3(4l(m^2g+1) + \sin(2\theta)\partial_\theta l) \\
&- 2\sin(\theta)(-2m(r_H-r)H_1(r\partial_r l + 2l) - \sin(\theta)(\partial_\theta H_3 \partial_\theta l + r(r-r_H)\partial_r H_3 \partial_r l) \\
&+ 2l(\cos(\theta)\partial_\theta H_3 + \sin(\theta)(r_H \partial_r H_3))) - 4mH_2(\sin(\theta)\partial_\theta l + 2\cos(\theta)l)) + 2r l^2(2\sin(\theta)((r_H-r)H_1 \\
&(r\partial_r \omega_m - \omega_m)(m\omega_m - r\omega) - H_2 \partial_\theta \omega_m(m\omega_m - r\omega) + r^2 \sin(\theta)\partial_r H_3 \omega_m \partial_r \omega_m + \sin(\theta)\partial_\theta H_3 \omega_m \partial_\theta \omega_m \\
&- rr_H \sin(\theta)\partial_r H_3 \omega_m \partial_r \omega_m - r \sin(\theta)\partial_r H_3 \omega_m^2 + r_H \sin(\theta)\partial_r H_3 \omega_m^2 + \cos(\theta)H_3 \omega_m \partial_\theta \omega_m + r^3 \partial_r \omega_m \partial_r V \\
&- r^2 r_H \partial_r \omega_m \partial_r V + r \partial_\theta \omega_m \partial_\theta V - r^2 \omega_m \partial_r V + rr_H \omega_m \partial_r V) - 2gH_3(m\omega_m - r\omega)^2)(4r(r_H-r)^2 f^2 l)^{-1}, \quad (B11)
\end{aligned}$$

$$\begin{aligned}
\partial_\theta^2 f + r(r-r_H)\partial_r^2 f &= \frac{1}{8} \left( (4\kappa \csc^2(\theta) (2r(r-r_H) \sin^2(\theta) (\partial_\theta H_1 - \partial_r H_2)^2 + g(2m^2 r(r-r_H)H_1^2 - 4mr(r-r_H) \sin(\theta)\partial_r H_3 H_1 \right. \\
&+ 2m^2 H_2^2 + \cos(2\theta)H_3^2 + H_3^2 - \cos(2\theta)\partial_\theta H_3^2 + \partial_\theta H_3^2 + r^2 \partial_r H_3^2 - rr_H \partial_r H_3^2 - r^2 \cos(2\theta)\partial_r H_3^2 + rr_H \cos(2\theta)\partial_r H_3^2 \\
&+ 2H_3 \sin(2\theta)\partial_\theta H_3 - 4mH_2(\cos(\theta)H_3 + \sin(\theta)\partial_\theta H_3)) f^2) (r^2 g l)^{-1} - \frac{4r_H \partial_r l f}{l} + (2 \csc(\theta) (4\kappa \sin(\theta)\partial_r V^2 r^4 \\
&- \frac{2\sin(\theta)\partial_r f \partial_r l r^4}{l} - 4r_H \kappa \sin(\theta)\partial_r V^2 r^3 - 8\sin(\theta)\partial_r f r^3 + \frac{4r_H \sin(\theta)\partial_r f \partial_r l r^3}{l} + 4\kappa \omega_m \partial_r H_3 \partial_r V r^3 \\
&- 4\kappa \cos(2\theta)\omega_m \partial_r H_3 \partial_r V r^3 + 4\kappa \csc(\theta)g(-\omega H_3 \sin(\theta) - mV)^2 r^2 + 4\kappa \sin(\theta)\partial_\theta V^2 r^2 + 3\kappa \omega_m^2 \sin(\theta)\partial_r H_3^2 r^2 \\
&- \kappa \omega_m^2 \sin(3\theta)\partial_r H_3^2 r^2 - 4\cos(\theta)\partial_\theta f r^2 - \frac{2\sin(\theta)\partial_\theta f \partial_\theta l r^2}{l} + 12r_H \sin(\theta)\partial_r f r^2 - \frac{2r_H^2 \sin(\theta)\partial_r f \partial_r l r^2}{l} \\
&- 4r_H \kappa \omega_m \partial_r H_3 \partial_r V r^2 + 4r_H \kappa \cos(2\theta)\omega_m \partial_r H_3 \partial_r V r^2 - 3r_H \kappa \omega_m^2 \sin(\theta)\partial_r H_3^2 r + r_H \kappa \omega_m^2 \sin(3\theta)\partial_r H_3^2 r \\
&+ 4(r-r_H)\kappa H_1^2(-r\omega + m\omega_m)^2 \sin(\theta)r + 4r_H \cos(\theta)\partial_\theta f r + \frac{2r_H \sin(\theta)\partial_\theta f \partial_\theta l r}{l} + 4\kappa H_3 \omega_m \sin(2\theta)\partial_\theta V r \\
&+ 4\kappa \omega_m \partial_\theta H_3 \partial_\theta V r - 4\kappa \cos(2\theta)\omega_m \partial_\theta H_3 \partial_\theta V r - 4r_H^2 \sin(\theta)\partial_r f r - 8(r-r_H)\kappa H_1(-r\omega + m\omega_m) \sin(\theta) \\
&(\omega_m \sin(\theta)\partial_r H_3 + r\partial_r V) r + 3\kappa \omega_m^2 \sin(\theta)\partial_\theta H_3^2 - \kappa \omega_m^2 \sin(3\theta)\partial_\theta H_3^2 + \kappa H_3^2 \omega_m^2 \sin(\theta) + 4\kappa H_2^2(-r\omega + m\omega_m)^2 \sin(\theta) \\
&+ \kappa H_3^2 \omega_m^2 \sin(3\theta) + 2\kappa \cos(\theta)H_3 \omega_m^2 \partial_\theta H_3 - 2\kappa \cos(3\theta)H_3 \omega_m^2 \partial_\theta H_3 - 8\kappa H_2(-r\omega + m\omega_m) \sin(\theta) (\cos(\theta)H_3 \omega_m \\
&+ \sin(\theta)\partial_\theta H_3 \omega_m + r\partial_\theta V)) (r(r-r_H))^{-1} + (8((r-r_H)(\partial_\theta f^2 + r(r-r_H)\partial_r f^2) + l(2\mu^2 \kappa g V^2 r^3 \\
&- 2\omega_m \sin(\theta)((r-r_H)\sin(\theta)\partial_r \omega_m - 2\mu^2 r \kappa g H_3 V(r,\theta))r + \sin^2(\theta)(\partial_\theta \omega_m^2 + r(r-r_H)\partial_r \omega_m^2))r \\
&+ (2\mu^2 r \kappa g H_3^2 + r-r_H)\omega_m^2 \sin^2(\theta))) ((r-r_H)f)^{-1}, \quad (B12)
\end{aligned}$$

$$\begin{aligned}
\partial_\theta^2 g + r(r-r_H)\partial_r^2 g &= \frac{1}{2} \left( -(\kappa f (6r(r-r_H) \sin^2(\theta) (\partial_\theta H_1 - \partial_r H_2)^2 - g(2m^2 r(r-r_H)H_1^2 - 4mr(r-r_H) \sin(\theta)\partial_r H_3 H_1 \right. \\
&+ 2m^2 H_2^2 + \cos(2\theta)H_3^2 + H_3^2 - \cos(2\theta)\partial_\theta H_3^2 + \partial_\theta H_3^2 + r^2 \partial_r H_3^2 - rr_H \partial_r H_3^2 - r^2 \cos(2\theta)\partial_r H_3^2 + rr_H \cos(2\theta)\partial_r H_3^2 \\
&+ 2H_3 \sin(2\theta)\partial_\theta H_3 - 4mH_2(\cos(\theta)H_3 + \sin(\theta)\partial_\theta H_3)) \csc^2(\theta) (r^2 l)^{-1} + 6\mu^2 \kappa g^2 H_3^2 + (r_H - 2r)\partial_r g \\
&+ \frac{2(\partial_\theta g^2 + r(r-r_H)\partial_r g^2)}{g} \\
&+ \frac{g(2\mu^2 r(r_H-r)\kappa H_1^2 l^2 - 2\mu^2 \kappa H_2^2 l^2 + 4\cot(\theta)\partial_\theta l l + 4r\partial_r l l - 2r_H \partial_r l l + \partial_\theta l^2 + r^2 \partial_r l^2 - rr_H \partial_r l^2)}{l^2} \\
&- (g((r-r_H)(\partial_\theta f^2 + r(r-r_H)f^2) + l(2\mu^2 \kappa g V^2 r^3 + 2\omega_m \sin(\theta)(2r \kappa g H_3 V \mu^2 + 3(r-r_H)\sin(\theta)\partial_r \omega_m) r \\
&- 3\sin^2(\theta)(\partial_\theta \omega_m^2 + r(r-r_H)\partial_r \omega_m^2) r + (2\mu^2 r \kappa g H_3^2 - 3r + 3r_H)\omega_m^2 \sin^2(\theta))) ((r-r_H)f)^{-1} \\
&+ (2g(\kappa \partial_r V^2 r^4 - r_H \kappa \partial_r V^2 r^3 + 2\kappa \omega_m \sin(\theta)\partial_r H_3 \partial_r V r^3 - 3\kappa \omega_m^2 g H_3^2 r^2 - 3m^2 \kappa \csc^2(\theta)g V^2 r^2 + \kappa \partial_\theta V^2 r^2 \\
&+ \kappa \omega_m^2 \sin^2(\theta)\partial_r H_3^2 r^2 - 6m\kappa \omega \csc(\theta)g H_3 V r^2 - r_H \partial_r f r^2 - 2r_H \kappa \omega_m \sin(\theta)\partial_r H_3 \partial_r V r^2 + (r-r_H)\kappa H_1^2(-r\omega + m\omega_m)^2 r \\
&- r_H \kappa \omega_m^2 \sin^2(\theta)\partial_r H_3^2 r + 2\kappa \cos(\theta)H_3 \omega_m \partial_\theta V r + 2\kappa \omega_m \sin(\theta)\partial_\theta H_3 \partial_\theta V r + r_H^2 \partial_r f r - 2(r-r_H)\kappa H_1(-r\omega + m\omega_m) \\
&(\omega_m \sin(\theta)\partial_r H_3 + r\partial_r V) r + \kappa \cos^2(\theta)H_3^2 \omega_m^2 + \kappa H_2^2(-r\omega + m\omega_m)^2 + \kappa \omega_m^2 \sin^2(\theta)\partial_\theta H_3^2 + \kappa H_3 \omega_m^2 \sin(2\theta)\partial_\theta H_3 \\
&- 2\kappa H_2(-r\omega + m\omega_m) (\cos(\theta)H_3 \omega_m + \sin(\theta)\partial_\theta H_3 \omega_m + r\partial_\theta V)) (r(r-r_H)f)^{-1}, \quad (B13)
\end{aligned}$$

$$\begin{aligned} \partial_\theta^2 l + r(r - r_H) \partial_r^2 l &= \frac{2\kappa(r - r_H)f(\partial_\theta H_1 - \partial_r H_2)^2}{rg} + \frac{2\kappa\mu^2 rgl^2(\sin(\theta)H_3\omega_m + rV)^2}{(r - r_H)f^2} + \frac{2\kappa rgl(-\omega H_3 - m \csc(\theta)V)^2}{(r - r_H)f} \\ &+ \frac{-4\kappa\mu^2 gH_3^2 l^2 + r^2 \partial_r l^2 + \partial_\theta l^2 - rr_H \partial_r l^2 + l(3(r_H - 2r)\partial_r l - 4 \cot(\theta)\partial_\theta l)}{2l}, \end{aligned} \quad (\text{B14})$$

$$\begin{aligned} \partial_\theta^2 \omega_m + r(r - r_H) \partial_r^2 \omega_m &= \frac{2(\partial_\theta f \partial_\theta \omega_m + (r - r_H) \partial_r f (r \partial_r \omega_m - \omega_m))}{f} + (\kappa \csc^2(\theta) f (-2r(r - r_H)H_1 \\ &(\sin(\theta) \partial_r H_3 (2m\omega_m - r\omega) + mr \partial_r V) + 2mr(r - r_H)H_1^2 (m\omega_m - r\omega) - 2H_2 (\sin(\theta) \partial_\theta H_3 (2m\omega_m - r\omega) \\ &+ \cos(\theta)H_3 (2m\omega_m - r\omega) + mr \partial_\theta V) + 2mH_2^2 (m\omega_m - r\omega) + r^2 \partial_r H_3^2 \omega_m - r^2 \cos(2\theta) \partial_r H_3^2 \omega_m + \partial_\theta H_3^2 \omega_m \\ &+ 2 \sin(2\theta)H_3 \partial_\theta H_3 \omega_m - \cos(2\theta) \partial_\theta H_3^2 \omega_m - rr_H \partial_r H_3^2 \omega_m + rr_H \cos(2\theta) \partial_r H_3^2 \omega_m + 2r^3 \sin(\theta) \partial_r H_3 \partial_r V \\ &- 2r^2 r_H \sin(\theta) \partial_r H_3 \partial_r V + 2r \sin(\theta) \partial_\theta H_3 \partial_\theta V + H_3^2 \omega_m + \cos(2\theta)H_3^2 \omega_m + 2r \cos(\theta)H_3 \partial_\theta V)) (r^2 l)^{-1} \\ &+ \frac{2\omega_m (\kappa\mu^2 r g H_3^2 + r - r_H)}{r} + 2\kappa\mu^2 r \csc(\theta) g H_3 V - \frac{3(\partial_\theta l \partial_\theta \omega_m + (r - r_H) \partial_r l (r \partial_r \omega_m - \omega_m))}{2l} \\ &- 3 \cot(\theta) \partial_\theta \omega_m + 2(r_H - r) \partial_r \omega_m. \end{aligned} \quad (\text{B15})$$

## 2. Boundary conditions

In order to solve the set of elliptic equations given above, we must impose boundary conditions, which we list here for completeness. The  $\theta$  boundary conditions follow from regularity at the poles and from the assumed symmetry across the  $\theta = \pi/2$  plane (equatorial symmetry), which is used to reduce the domain to  $0 < \theta < \pi/2$ . At  $\theta = 0$  the boundary conditions are

$$\begin{aligned} \partial_\theta f = \partial_\theta l = \partial_\theta \omega_m = V = H_1 = \partial_\theta H_2 = \partial_\theta H_3 = \phi = 0, \\ g = 1, \end{aligned}$$

and at the  $\theta = \pi/2$  boundary we have

$$\begin{aligned} \partial_\theta f = \partial_\theta g = \partial_\theta l = \partial_\theta \omega_m = \partial_\theta V = \partial_\theta H_1 \\ = H_2 = \partial_\theta H_3 = \partial_\theta \phi = 0. \end{aligned}$$

In the radial direction, the boundary at the black hole horizon can be derived by using Frobenius's method applied to the equations listed in Sec. B1 (along with the synchronicity condition), while those at spatial infinity ( $x = 1$ ) follow from the assumption of asymptotic flatness. For the  $r = r_H$  (the black hole horizon) boundary, we find

$$\partial_r f = \partial_r g = \partial_r l = \partial_r H_i = \partial_r \phi = 0, \quad (\text{B16})$$

$$\omega_m = m\Omega_H, \quad (\text{B17})$$

$$\left(V + \frac{\omega}{m} H_3 \sin \theta\right) = 0, \quad (\text{B18})$$

while at the  $r = \infty$  boundary we find

$$f = g = l = 1, \quad \omega_m = V = H_i = \phi = 0.$$

In the scalar case, the above boundary conditions are equivalent to those in Ref. [49]. In the vector case, the boundary conditions are equivalent to those in Ref. [50], with the exception of the condition on the  $H_1$  matter field at the black hole's horizon:  $\partial_r H_1(r_H) = 0$  [c.f. Ref. [50] which lists  $H_1(r_H) = 0$ ].

## 3. Seeding solutions

We discretize the elliptic equations given above with fifth-order accurate finite difference stencils, and solve them using Newton-Raphson relaxation. The relaxation method requires a sufficiently good initial guess for the field values in order to converge. In the scalar case, we use a numerical solution from Ref. [49] as an initial guess when solving for one point in the parameter space (and find a consistent solution), and then find subsequent solutions by slowly varying the parameters of the system while using the previous solution as an initial guess.

In the vector case, we instead <sup>10</sup> seed vector solutions using the analytic solution in the non-relativistic limit [24] superimposed with a Kerr solution for the metric (see Ref. [49] Appendix A for a description of the Kerr metric in these coordinates). In the non-relativistic limit, the vector matter fields have the solution:

$$\begin{aligned} V &= -\frac{\exp(-r\alpha)\alpha^{5/2} \sin(\theta)}{2\sqrt{\pi}\omega} & H_1 &= \frac{\exp(-r\alpha)\alpha^{3/2} \sin(\theta)}{2\sqrt{\pi}} \\ H_2 &= \frac{\exp(-r\alpha)r\alpha^{3/2} \cos(\theta)}{2\sqrt{\pi}} & H_3 &= \frac{\exp(-r\alpha)r\alpha^{3/2}}{2\sqrt{\pi}}. \end{aligned} \quad (\text{B19})$$

We note that there are multiple solutions that satisfy the symmetry conditions that we impose here. These solutions can be labelled by mode number  $n$ , where the different behaviour of the  $n = 0$  and  $n = 1$  solutions is

<sup>10</sup> Relativistic solutions for black hole-vector boson clouds are given in Ref. [51], though we were unable to use them to relax to a solution to our equations, which could be related to the difference in boundary conditions discussed above. However, our solutions do seem equivalent in that the extracted black hole and cloud masses are equivalent for the same choice of frequency and black hole radius.

discussed in Ref. [51]. Here we are interested in the fundamental  $n = 0$  mode (which grows the fastest through superradiance when  $m = 1$ ), which can be identified by the absence of nodes in the  $V$  component of the matter solution.

### Appendix C: Quantifying Errors in Frequency Shift

In this section, we provide details on how the errors in the cloud mass-dependent shift in the oscillation frequency are estimated. There are multiple sources of error in the frequency shift calculation. The main sources are the following:

- The complex field approximation
- Numerical error in individual solutions
- Interpolation error

We take the overall relative error to be

$$\frac{\delta\omega}{\Delta\omega} = |E_{\text{theoretical}}| + |E_{\text{numerical}}| + |E_{\text{fit}}|, \quad (\text{C1})$$

where  $E_{\text{theoretical}}$  is the relative error due to the complex field or oscillation-average approximation,  $E_{\text{numerical}}$  is the error from the extraction of physical quantities from each numerical solution, and  $E_{\text{fit}}$  is the interpolation error. The results of these estimates are shown in Fig. 8. We outline the calculation of each of these contributions to the overall error in the following.

#### 1. Complex field approximation

##### a. Comparing Newtonian limit term

As discussed in Sec. II C, we make an axisymmetric or oscillation-averaged approximation to reduce the dimensionality of the problem. The theoretical error arising from making such an approximation can be obtained by comparing the stress-energy tensors of the full complex-field  $\Phi$  solution to that of a real-field solution  $\psi$ . To that end, we obtain a real-field solution by taking the real part of the complex field configuration (adjusted by a factor of  $\sqrt{2}$  to obtain a field with the same total energy), such that  $\psi = \sqrt{2}\text{Re}(\Phi)$ . In the vector case, we proceed in the same way, with  $\mathcal{A}_a = \sqrt{2}\text{Re}(A_a)$ .

Since the self-gravity correction scales with the binding energy of the cloud [24, 41] (in the Newtonian limit), we will use that quantity to estimate the theoretical error. We introduce the quantity  $W^{\ell \leq l'}$ , defined as the  $l'$  multipole approximation of the non-relativistic binding

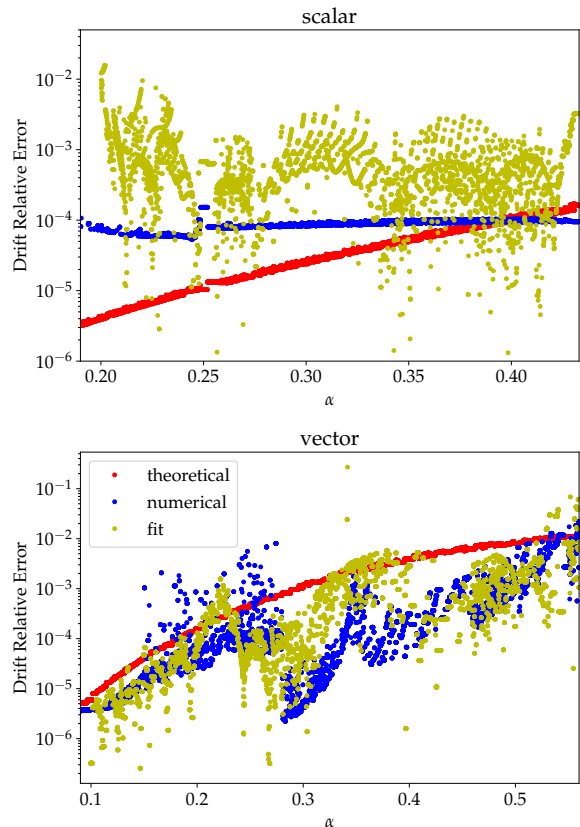


Figure 8: Estimated errors in the extracted frequency shift relative to the non-relativistic limit of the frequency shift. We compare the final numerical error in each solution to the estimated theoretical error due to our oscillation averaged approximation, as well as the interpolation error. Here, the numerical and interpolation errors are plotted for solutions with  $M_{\text{cloud}}/M_{\text{BH}} > 1\%$  to avoid issues with relative error becoming larger as the frequency shift goes to zero.

energy,

$$W^{\ell \leq l'} = - \int d^3\mathbf{r} \int_{|\mathbf{r}'| < |\mathbf{r}|} d^3\mathbf{r}' \rho(\mathbf{r}) \rho(\mathbf{r}') \times \quad (\text{C2})$$

$$\sum_{l=0}^{l'} \sum_{m=-l}^l \left( \frac{|\mathbf{r}'|^l}{|\mathbf{r}|^{l+1}} \right) \frac{4\pi}{2l+1} Y_{lm}(\Omega) Y_{lm}^*(\Omega'), \quad (\text{C3})$$

which is obtained by applying a truncated version of the sum given in Eq. (7) to the expression for  $W$  given in Eq. (6). In computing the above expressions, we use the energy density measured with respect to an observer whose four velocity  $n_a$  is normal to slices of constant time

$$\rho = n_a n_b T^{ab}. \quad (\text{C4})$$

For the volume element, we take  $d^3\mathbf{r} = \sqrt{\gamma} d^3x$ , where  $\gamma$  is the determinant from the induced spatial metric in our coordinates [see Eq. (B1)]. We then estimate the

theoretical error to be

$$E_{\text{theoretical}} \approx \frac{|W_{\text{Re}}^{\ell \leq 2} - W_{\text{C}}^{\ell \leq 2}|}{W_{\text{C}}^{\ell \leq 0}}, \quad (\text{C5})$$

where ‘‘Re’’ and ‘‘C’’ indicate the quantity computed with the stress-energy tensors corresponding to the real and complex solutions ( $\psi$  and  $\Phi$  in the scalar case, or  $\mathcal{A}_a$  and  $A_a$  in the vector case), respectively. In either case, the metric is taken to be identical and equal to that of the full stationary and axisymmetric spacetime. This calculation estimates the error in a non-relativistic approximation of the self-gravity of the cloud, the binding energy, calculated up to the  $l = 2$  multipole. We calculate the next non-trivial multipole in the scalar case ( $l = 3$ ) and find it to be subdominant to the  $l = 2, m = 2$  contribution at the ratio of  $10^{-5}$  at  $\alpha = 0.5$ , indicating even higher multipoles are negligible.

Using the estimate (C5), we obtain sub-percent level errors across the parameter space in the vector case, and errors of at most  $O(10^{-4})$  in the scalar case, as can be seen in Fig. 8. This error estimate is a non-relativistic approximation in both spin cases, and should only be fully accurate in that limit. Because it is a leading order calculation, it will not capture the more quickly growing contributions at higher orders in  $\alpha$ , and thus may underestimate the error due to this approximation at high  $\alpha$ . However, here we are mainly using it to estimate the relative contribution of non-axisymmetric components of the cloud’s energy to the self-gravity. We further note that Ref. [47] estimates the frequency shift for the scalar case using relativistic black hole perturbation theory, but with a semi-Newtonian approximation for the gravitational potential and finds results noticeably closer to the relativistic ones presented here than to the leading order non-relativistic result, suggesting that the frequency shift is well described by taking some leading order non-relativistic terms. This further motivates us to use our non-relativistic estimate for the theoretical error in taking an oscillation-averaged approximation, even at higher  $\alpha$ . As can be seen in Fig. 8, the theoretical error is comparable or subdominant to other sources of error in most of the parameter space, and so the exact value of the theoretical error here (up to a factor of a few) does not dramatically impact the total error estimate.

### b. Comparing to numerical relativity

In addition to calculating a non-relativistic estimate of the theoretical error as is described in the last section, we can also compare to the numerical relativity simulation considered in Ref. [75]. That study evolved the full Einstein-Proca equations, without symmetry assumptions, through the saturation of the superradiant instability and into the phase where the cloud dissipates through gravitational radiation for one case where initially  $\chi_{\text{BH}} = 0.99$  and  $\alpha = 0.4$ , leading to a vector boson

cloud that peaks at  $M_{\text{cloud}} \approx 0.06M_{\text{BH}}$ . We compare the gravitational wave frequency found in that study to the test-field frequency with the non-relativistic frequency shift and fully relativistic frequency shift estimate (using the estimates of the black hole and cloud properties found in the simulation) in Fig. 9. We find an improved agreement with numerical relativity, compared to the test non-relativistic shift estimate, when the relativistic frequency shift calculation is included in the waveform. Considering the expected numerical error in the simulations, as well as the fact that there is a small spurious excitation of the first overtone mode as discussed in Ref. [75], which will bias the frequency upwards, the difference, at the level of 0.1%, is within the expected bounds.

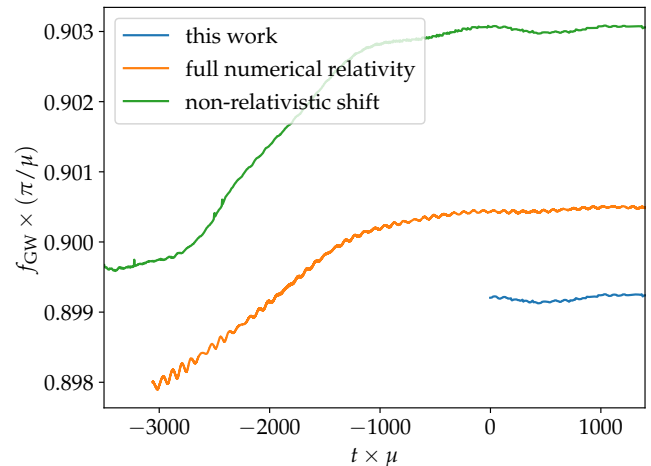


Figure 9: The frequency of gravitational waves from an oscillating vector boson cloud around a black hole is compared in three cases. The numerical relativity result (averaged over a number of oscillations) is from a simulation including the growth period of the cloud from Ref. [76], and the other two results are using the test field frequency calculation from Ref. [45], and the leading order non-relativistic frequency shift or the relativistic frequency shift as is calculated here. Here, the superradiant instability phase ends at  $t = 0$ , after which this frequency shift calculation is valid.

## 2. Numerical error in solutions

We quantify the numerical error  $E_{\text{numerical}}$  using a combination of errors in the extracted physical quantities. For the frequency fit, the frequency is a fixed input parameter, and the only extracted quantities are the black hole mass and the cloud mass (described in Appendix A). We approximate the relative numerical error in a particular solution by the sum of the relative errors in both the cloud and black hole mass.

We establish the numerical errors in each mass calculation by performing convergence studies. The elliptic



solver uses sixth order finite differencing and so the solution in the bulk converges at sixth order. To calculate the mass of the black hole we sometimes use an extrapolation to the horizon point (as described in Appendix A), and so have slower convergence.

In the scalar case, we perform a convergence test using three resolutions differing by a factor of 2/3. We find second order convergence in the horizon black hole mass and sixth order convergence in the cloud mass, and we perform Richardson extrapolation to find an overall error. In this case, the black hole mass dominates the numerical error at small  $\alpha$ . The reason the black hole mass converges so slowly is because its calculation relies on an extrapolation to the boundary, where the extrapolation error is dominating over the error in each point in the bulk. For the final fit, we use a resolution of  $n_x = 391$  radial points and  $n_\theta = 46$  angular points. The result of this analysis is shown in comparison with the other sources of error in the top panel in Fig. 8.

In the vector case we perform a convergence test using three resolutions differing by a factor of 3/4 (where our numerical resolution of  $n_x = 261$  and  $n_\theta = 35$  is the highest resolution). We find sixth order convergence in the ADM mass and cloud mass, with second order convergence in the horizon black hole mass. We perform Richardson extrapolation to find an overall error. In this case the horizon black hole mass has good convergence at low  $\alpha$ , but stops being well resolved at high  $\alpha$  ( $\alpha > 0.4$ ), whereas the ADM mass converges well at high  $\alpha$ , but stops converging at these resolutions when the cloud becomes bigger, and closer to the compactified boundary, at  $\alpha < 0.2$ <sup>11</sup>. For  $\alpha > 0.22$ , we use a resolution of  $n_x = 261$  and  $n_\theta = 35$ , and the ADM and cloud mass calculations. We use the horizon black hole mass instead of the ADM mass as well as higher resolution points for  $\alpha < 0.22$ , with varying resolution so as to make the estimated numerical errors comparable to the theoretical error in that regime. The final error estimates are shown in Fig. 8. We perform a fit for the frequency shift for three different resolutions of points, and find convergence in the overall fit parameters for the frequency shift as well as in each solution.

There is also some contribution to the overall error from the interpolation between solutions. We evaluate this error  $E_{\text{fit}}$  by removing each point in turn from the interpolation and calculating the difference between the interpolation and that point. We show the results of this test for the scalar and vector cases in Fig. 8.

<sup>11</sup> We check the convergence using a similar study but where the minimum resolution is  $n_x = 347$  and  $n_\theta = 47$ , and find that the ADM mass converges as expected for  $\alpha > 0.13$ .

### 3. Extrapolation to non-relativistic solutions

As described in Sec. III, to extrapolate to small  $\alpha$  we fit the self gravity correction to the cloud frequency using a polynomial in  $M_{\text{cloud}}/M_{\text{BH}}$  and  $\alpha$ . We use points with  $0.2 < \alpha < 0.3$  in the scalar case and  $0.09 < \alpha < 0.14$  in the vector case. By construction, this polynomial reduces to the non-relativistic result to leading order in the  $\alpha \ll 1$  limit. It only remains to quantify the error in the polynomial fit. We do this by first calculating the maximum deviation of the polynomial fit from the full spline interpolation of the data points in the fit region,  $\Delta_{\text{fit}}$ . Then the maximum error in the coefficient for the leading order relativistic correction to the shift is  $\delta c_{3,1} = \Delta_{\text{fit}}\alpha^{-3}$ . So we can extrapolate the relative error in the frequency shift to lower values of  $\alpha$  using

$$\frac{\delta\omega}{\Delta\omega} = \frac{\delta c_{3,1}\alpha^3}{C_{\text{nr}}\alpha^2} = \frac{\Delta_{\text{fit}}\alpha}{C_{\text{nr}}} \quad (\text{C6})$$

for  $\alpha$  below the regime where we have numerical results. In the each spin case we find that the polynomial fit to the data is close to the numerical error for the nearby small  $\alpha$  points.

### Appendix D: Calculating Light Ring and ISCO

We find the equatorial light ring by solving the radial geodesic equation together with the normalization of the four velocity. We interpolate our numerical solution between grid points before solving for the radius that gives circular orbits<sup>12</sup>. We use the proper circumferential radius to convert our measured light-ring to standard coordinates

$$R = \frac{1}{2\pi} \int d\varphi \sqrt{g_{\varphi\varphi}(r, \theta = \pi/2)}. \quad (\text{D1})$$

We calculate the equatorial ISCO by solving the radial geodesic equation, varying the conserved quantities  $E = -t_a u^a$  and  $L = \phi_a u^a$  (where  $u^a$  is a time-like geodesic four velocity,  $t^a$  is the stationary Killing vector and  $\phi^a$  is the axial Killing vector) and the estimated ISCO radius to minimize simultaneously  $\dot{r}$ ,  $\partial\dot{r}/\partial r$ , and  $\partial^2\dot{r}/\partial r^2$ . The resulting solution gives the ISCO radius, as well as  $E$  and  $L$  which can be mapped to the four velocity  $u^a$  of a particle travelling along the ISCO. This four velocity can then be used to calculate the ISCO orbital frequency as well as the frequency of light measured by that observer. We use the proper time measured by an observer orbiting on the ISCO to define a coordinate independent orbit frequency,

$$\Omega = \frac{d\varphi}{d\tau}. \quad (\text{D2})$$

<sup>12</sup> We use a cubic spline interpolation and an optimisation algorithm from `scipy`.

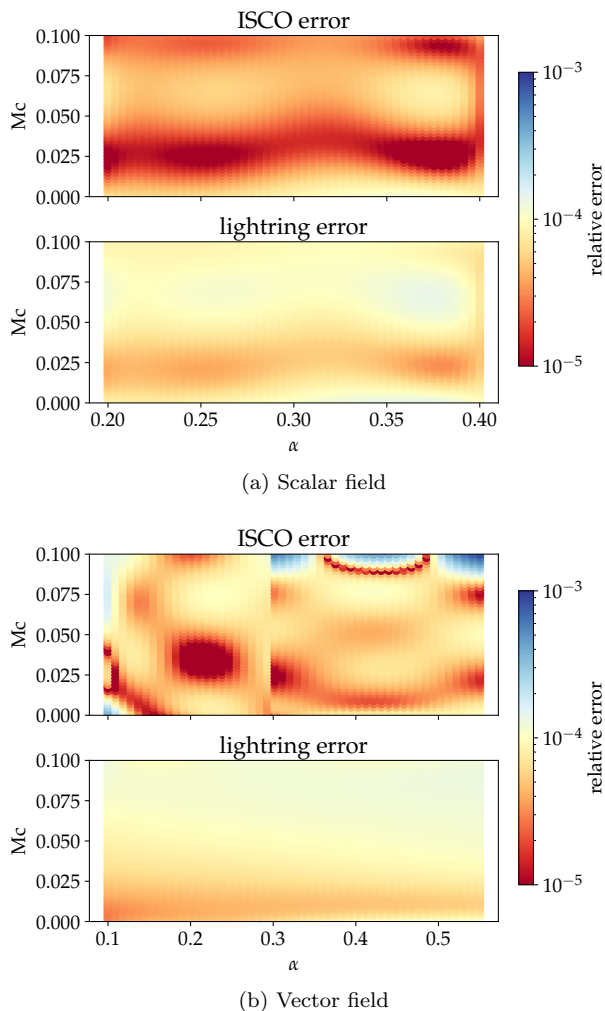


Figure 10: We perform a convergence test to determine the numerical error in the position of the lightring and ISCO. The relative error in the circumferential radius is shown here for both scalar and vector clouds. The feature at  $\alpha = 0.3$  in the ISCO radius for the vector case is due to a change in the convergence order from 6th order at high  $\alpha$  to second order for low  $\alpha$ .

The frequency of light measured by that observer is  $\omega = -u^a k_a$ , where  $k^a$  is the four velocity of the light being measured. We choose two initial directions for light  $k^a$  being emitted from the ISCO, such that in both cases the light is emitted equatorially and the initial radial component is zero.

Errors in the light ring and ISCO calculations are evaluated using a convergence test and Richardson extrapolation, with results shown in Fig. 10. As can be seen there,

the relative errors are always  $< 10^{-3}$  and are  $\lesssim 10^{-4}$  except in some corner of the vector boson parameter space.

## Appendix E: Consistency checks

### 1. Test field limit

We confirm that in the test field limit our results match those in the literature. We do this by comparing our fit to the constant in cloud mass part of the frequency with the test field calculation in Ref. [45]. The results of this comparison are shown in Fig. 11. We find agreement within the expected error bars of our calculation.

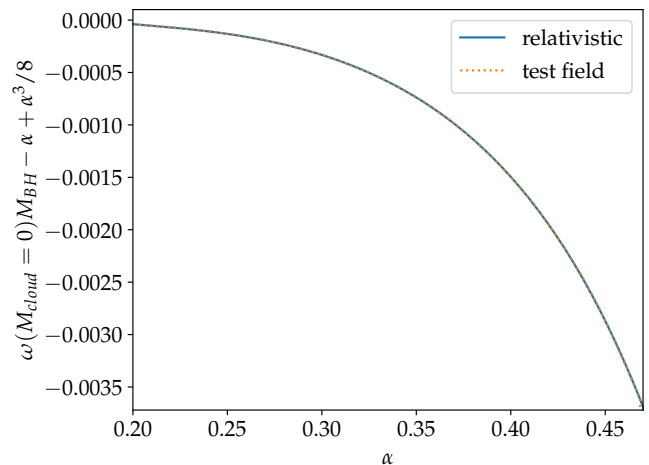


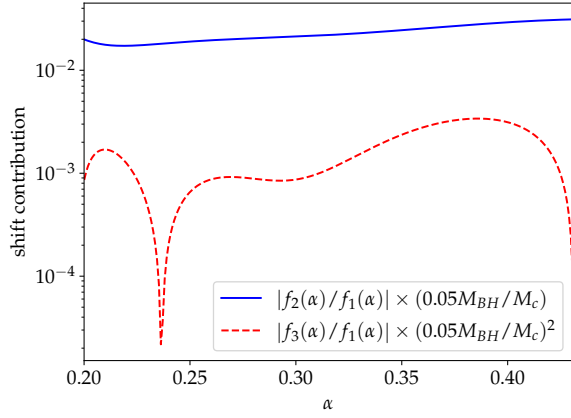
Figure 11: We show the relativistic correction to the frequency in the test field limit and confirm that our result matches that from the test field calculations in Ref. [45]. This example is from the scalar case, but we see a similar agreement in the vector case.

### 2. Nonlinear dependence of frequency on $M_{\text{cloud}}$

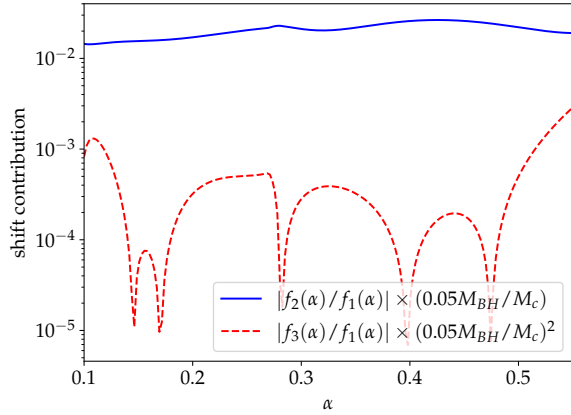
As described in Sec. III B, when fitting for the cloud mass dependent part of the frequency, we include a term linear in cloud mass as well as a quadratic term in the fit to the frequency shift. As shown in Fig. 12, the quadratic term corrects the linear term only at the level of a few percent, even when the cloud is significant. We find that including an additional cubic in cloud mass term does not significantly decrease the root mean squared error in the fit, and, as is shown in Fig. 12, that term is oscillating around zero and does not appear to be well resolved.

[1] R. Peccei and H. R. Quinn, *Phys. Rev. Lett.* **38**, 1440 (1977).  
 [2] S. Weinberg, *Phys. Rev. Lett.* **40**, 223 (1978).

[3] G. G. Raffelt, *Lect. Notes Phys.* **741**, 51 (2008), arXiv:hep-ph/0611350.



(a) Scalar field



(b) Vector field

Figure 12: The contribution to the frequency shift of the second order in cloud mass term, relative to linear term, when the cloud mass is  $M_{\text{cloud}}/M_{\text{BH}} = 0.05$ . We also include a comparison for the value of a third order term when it is included in the fit described in Eq. (17). When this third order term is included, it is found to contribute at below the estimated error. The feature at  $\alpha = 0.275$  in panel (b) is due to an interpolation between fits to data at different resolutions.

- [4] J. E. Kim and G. Carosi, *Rev. Mod. Phys.* **82**, 557 (2010), [Erratum: *Rev.Mod.Phys.* 91, 049902 (2019)], arXiv:0807.3125 [hep-ph].
- [5] A. Arvanitaki and S. Dubovsky, *Phys. Rev. D* **83**, 044026 (2011), arXiv:1004.3558 [hep-th].
- [6] L. Hui, J. P. Ostriker, S. Tremaine, and E. Witten, *Phys. Rev. D* **95**, 043541 (2017), arXiv:1610.08297 [astro-ph.CO].
- [7] B. Holdom, *Phys. Lett.* **B166**, 196 (1986).
- [8] P. Pani, V. Cardoso, L. Gualtieri, E. Berti, and A. Ishibashi, *Phys. Rev.* **D86**, 104017 (2012), arXiv:1209.0773 [gr-qc].
- [9] P. W. Graham, J. Mardon, and S. Rajendran, *Phys. Rev. D* **93**, 103520 (2016), arXiv:1504.02102 [hep-ph].
- [10] P. Agrawal, N. Kitajima, M. Reece, T. Sekiguchi, and F. Takahashi, *Phys. Lett. B* **801**, 135136 (2020), arXiv:1810.07188 [hep-ph].
- [11] A. Arvanitaki, S. Dimopoulos, S. Dubovsky, N. Kaloper, and J. March-Russell, *Phys. Rev. D* **81**, 123530 (2010), arXiv:0905.4720 [hep-th].
- [12] M. Goodsell, J. Jaeckel, J. Redondo, and A. Ringwald, *JHEP* **11**, 027 (2009), arXiv:0909.0515 [hep-ph].
- [13] Y. B. Zel'Dovich, *Soviet Journal of Experimental and Theoretical Physics Letters* **14**, 180 (1971).
- [14] C. W. Misner, *Phys. Rev. Lett.* **28**, 994 (1972).
- [15] A. A. Starobinsky, *Sov. Phys. JETP* **37**, 28 (1973).
- [16] R. Brito, V. Cardoso, and P. Pani, *Phys. Rev. D* **88**, 023514 (2013), arXiv:1304.6725 [gr-qc].
- [17] O. J. C. Dias, G. Lingetti, P. Pani, and J. E. Santos, *Phys. Rev. D* **108**, L041502 (2023), arXiv:2304.01265 [gr-qc].
- [18] E. Babichev and A. Fabbri, *Class. Quant. Grav.* **30**, 152001 (2013), arXiv:1304.5992 [gr-qc].
- [19] W. E. East and N. Siemonsen, *Phys. Rev. D* **108**, 124048 (2023), arXiv:2309.05096 [gr-qc].
- [20] A. Arvanitaki, M. Baryakhtar, and X. Huang, *Phys. Rev. D* **91**, 084011 (2015), arXiv:1411.2263 [hep-ph].
- [21] A. Arvanitaki, M. Baryakhtar, S. Dimopoulos, S. Dubovsky, and R. Lasenby, *Phys. Rev. D* **95**, 043001 (2017), arXiv:1604.03958 [hep-ph].
- [22] V. Cardoso, O. J. C. Dias, G. S. Hartnett, M. Middleton, P. Pani, and J. E. Santos, *JCAP* **03**, 043 (2018), arXiv:1801.01420 [gr-qc].
- [23] K. K. Y. Ng, S. Vitale, O. A. Hannuksela, and T. G. F. Li, *Phys. Rev. Lett.* **126**, 151102 (2021), arXiv:2011.06010 [gr-qc].
- [24] M. Baryakhtar, R. Lasenby, and M. Teo, *Phys. Rev. D* **96**, 035019 (2017), arXiv:1704.05081 [hep-ph].
- [25] M. J. Stott, (2020), arXiv:2009.07206 [hep-ph].
- [26] J. Aasi *et al.* (LIGO Scientific), *Class. Quant. Grav.* **32**, 074001 (2015), arXiv:1411.4547 [gr-qc].
- [27] F. Acernese *et al.* (VIRGO), *Class. Quant. Grav.* **32**, 024001 (2015), arXiv:1408.3978 [gr-qc].
- [28] Y. Aso, Y. Michimura, K. Somiya, M. Ando, O. Miyakawa, T. Sekiguchi, D. Tatsumi, and H. Yamamoto (KAGRA), *Phys. Rev. D* **88**, 043007 (2013), arXiv:1306.6747 [gr-qc].
- [29] T. Akutsu *et al.* (KAGRA), *PTEP* **2021**, 05A101 (2021), arXiv:2005.05574 [physics.ins-det].
- [30] P. Amaro-Seoane *et al.* (LISA), (2017), arXiv:1702.00786 [astro-ph.IM].
- [31] R. Abbott *et al.* (LIGO Scientific, Virgo, KAGRA), *Phys. Rev. D* **105**, 102001 (2022), arXiv:2111.15507 [astro-ph.HE].
- [32] L. Tsukada, T. Callister, A. Matas, and P. Meyers, *Phys. Rev. D* **99**, 103015 (2019), arXiv:1812.09622 [astro-ph.HE].
- [33] L. Tsukada, R. Brito, W. E. East, and N. Siemonsen, *Phys. Rev. D* **103**, 083005 (2021), arXiv:2011.06995 [astro-ph.HE].
- [34] C. Palomba *et al.*, *Phys. Rev. Lett.* **123**, 171101 (2019), arXiv:1909.08854 [astro-ph.HE].
- [35] R. Abbott *et al.* (KAGRA, LIGO Scientific, VIRGO), *Phys. Rev. D* **106**, 042003 (2022), arXiv:2204.04523 [astro-ph.HE].
- [36] R. Brito, S. Ghosh, E. Barausse, E. Berti, V. Cardoso, I. Dvorkin, A. Klein, and P. Pani, *Phys. Rev. D* **96**, 064050 (2017), arXiv:1706.06311 [gr-qc].

- [37] H. Yoshino and H. Kodama, *PTEP* **2015**, 061E01 (2015), [arXiv:1407.2030 \[gr-qc\]](#).
- [38] R. Brito, S. Ghosh, E. Barausse, E. Berti, V. Cardoso, I. Dvorkin, A. Klein, and P. Pani, *Phys. Rev. Lett.* **119**, 131101 (2017), [arXiv:1706.05097 \[gr-qc\]](#).
- [39] S. J. Zhu, M. Baryakhtar, M. A. Papa, D. Tsuna, N. Kawanaka, and H.-B. Eggenstein, *Phys. Rev. D* **102**, 063020 (2020), [arXiv:2003.03359 \[gr-qc\]](#).
- [40] L. Sun, R. Brito, and M. Isi, *Phys. Rev. D* **101**, 063020 (2020), [Erratum: *Phys.Rev.D* 102, 089902 (2020)], [arXiv:1909.11267 \[gr-qc\]](#).
- [41] M. Isi, L. Sun, R. Brito, and A. Melatos, *Phys. Rev. D* **99**, 084042 (2019), [Erratum: *Phys.Rev.D* 102, 049901 (2020)], [arXiv:1810.03812 \[gr-qc\]](#).
- [42] K. H. M. Chan and O. A. Hannuksela, *Phys. Rev. D* **109**, 023009 (2024), [arXiv:2209.03536 \[gr-qc\]](#).
- [43] D. Jones, L. Sun, N. Siemonsen, W. E. East, S. M. Scott, and K. Wette, *Phys. Rev. D* **108**, 064001 (2023), [arXiv:2305.00401 \[gr-qc\]](#).
- [44] M. Baryakhtar, M. Galanis, R. Lasenby, and O. Simon, *Phys. Rev. D* **103**, 095019 (2021), [arXiv:2011.11646 \[hep-ph\]](#).
- [45] N. Siemonsen, T. May, and W. E. East, *Phys. Rev. D* **107**, 104003 (2023), [arXiv:2211.03845 \[gr-qc\]](#).
- [46] N. Siemonsen and W. E. East, *Phys. Rev. D* **101**, 024019 (2020), [arXiv:1910.09476 \[gr-qc\]](#).
- [47] E. Cannizzaro, L. Sberna, S. R. Green, and S. Hollands, *Phys. Rev. Lett.* **132**, 051401 (2024), [arXiv:2309.10021 \[gr-qc\]](#).
- [48] C. A. R. Herdeiro and E. Radu, *Phys. Rev. Lett.* **112**, 221101 (2014), [arXiv:1403.2757 \[gr-qc\]](#).
- [49] C. Herdeiro and E. Radu, *Class. Quant. Grav.* **32**, 144001 (2015), [arXiv:1501.04319 \[gr-qc\]](#).
- [50] C. Herdeiro, E. Radu, and H. Rúnarsson, *Class. Quant. Grav.* **33**, 154001 (2016), [arXiv:1603.02687 \[gr-qc\]](#).
- [51] N. M. Santos, C. L. Benone, L. C. B. Crispino, C. A. R. Herdeiro, and E. Radu, *JHEP* **07**, 010 (2020), [arXiv:2004.09536 \[gr-qc\]](#).
- [52] Y. Ni, M. Zhou, A. Cardenas-Avendano, C. Bambi, C. A. R. Herdeiro, and E. Radu, *JCAP* **07**, 049 (2016), [arXiv:1606.04654 \[gr-qc\]](#).
- [53] I. Sengo, P. V. P. Cunha, C. A. R. Herdeiro, and E. Radu, *JCAP* **01**, 047 (2023), [arXiv:2209.06237 \[gr-qc\]](#).
- [54] S. L. Detweiler, *Phys. Rev. D* **22**, 2323 (1980).
- [55] H. Yoshino and H. Kodama, *PTEP* **2014**, 043E02 (2014), [arXiv:1312.2326 \[gr-qc\]](#).
- [56] R. Brito, V. Cardoso, and P. Pani, *Class. Quant. Grav.* **32**, 134001 (2015), [arXiv:1411.0686 \[gr-qc\]](#).
- [57] N. Siemonsen and W. E. East, *Phys. Rev. D* **103**, 044022 (2021), [arXiv:2011.08247 \[gr-qc\]](#).
- [58] R. Abbott *et al.* (KAGRA, VIRGO, LIGO Scientific), *Phys. Rev. X* **13**, 041039 (2023), [arXiv:2111.03606 \[gr-qc\]](#).
- [59] L. Lindblom, B. J. Owen, and D. A. Brown, *Phys. Rev. D* **78**, 124020 (2008), [arXiv:0809.3844 \[gr-qc\]](#).
- [60] R. L. Arnowitt, S. Deser, and C. W. Misner, *Phys. Rev.* **116**, 1322 (1959).
- [61] J. E. McClintock, R. Narayan, and J. F. Steiner, *Space Sci. Rev.* **183**, 295 (2014), [arXiv:1303.1583 \[astro-ph.HE\]](#).
- [62] C. S. Reynolds, *Nature Astron.* **3**, 41 (2019), [arXiv:1903.11704 \[astro-ph.HE\]](#).
- [63] C. S. Reynolds, *Space Sci. Rev.* **183**, 277 (2014), [arXiv:1302.3260 \[astro-ph.HE\]](#).
- [64] Y. Chen, X. Xue, R. Brito, and V. Cardoso, *Phys. Rev. Lett.* **130**, 111401 (2023), [arXiv:2211.03794 \[gr-qc\]](#).
- [65] H. Fukuda and K. Nakayama, *JHEP* **01**, 128 (2020), [arXiv:1910.06308 \[hep-ph\]](#).
- [66] W. E. East, *Phys. Rev. Lett.* **129**, 141103 (2022), [arXiv:2205.03417 \[hep-ph\]](#).
- [67] W. E. East and J. Huang, *JHEP* **12**, 089 (2022), [arXiv:2206.12432 \[hep-ph\]](#).
- [68] H. S. Chia, C. Doorman, A. Wernersson, T. Hinderer, and S. Nissanke, *JCAP* **04**, 018 (2023), [arXiv:2212.11948 \[gr-qc\]](#).
- [69] N. Siemonsen, C. Mondino, D. Egana-Ugrinovic, J. Huang, M. Baryakhtar, and W. E. East, (2022), [arXiv:2212.09772 \[astro-ph.HE\]](#).
- [70] H. Omiya, T. Takahashi, T. Tanaka, and H. Yoshino, *JCAP* **06**, 016 (2023), [arXiv:2211.01949 \[gr-qc\]](#).
- [71] H. Omiya, T. Takahashi, T. Tanaka, and H. Yoshino, *Phys. Rev. D* **110**, 044002 (2024), [arXiv:2404.16265 \[gr-qc\]](#).
- [72] S. Collaviti, L. Sun, M. Galanis, and M. Baryakhtar, (2024), [arXiv:2407.04304 \[gr-qc\]](#).
- [73] C. A. R. Herdeiro, E. Radu, and H. Rúnarsson, *Phys. Rev. D* **92**, 084059 (2015), [arXiv:1509.02923 \[gr-qc\]](#).
- [74] M. Khalaf, E. Kuflik, A. Lenoci, and N. C. Stone, (2024), [arXiv:2408.16051 \[astro-ph.CO\]](#).
- [75] W. E. East, *Phys. Rev. Lett.* **121**, 131104 (2018), [arXiv:1807.00043 \[gr-qc\]](#).
- [76] W. E. East and F. Pretorius, *Phys. Rev. Lett.* **119**, 041101 (2017), [arXiv:1704.04791 \[gr-qc\]](#).